The Canadian Mineralogist
Vol. 58, pp. 477-509 (2020)
DOI: 10.3749/canmin.1900063

WINDMOUNTAINITE, $\square Fe^{3+}_2Mg_2\square_2Si_8O_{20}(OH)_2(H_2O)_4{\cdot}4H_2O$, A NEW MODULATED, LAYERED Fe^{3+}-Mg-SILICATE-HYDRATE FROM WIND MOUNTAIN, NEW MEXICO: CHARACTERIZATION AND ORIGIN, WITH COMMENTS ON THE CLASSIFICATION OF PALYGORSKITE-GROUP MINERALS

DEREK D. LEUNG[§] AND ANDREW M. MCDONALD

Harquail School of Earth Sciences, Laurentian University, 935 Ramsey Lake Road, Sudbury, Ontario P3E 2C6, Canada

ABSTRACT

Windmountainite, ideally $\square Fe^{3+}_2Mg_2\square_2Si_8O_{20}(OH)_2(H_2O)_4{\cdot}4H_2O$, is a new mineral species and member of the palygorskite group discovered as orange-brown, radiating aggregates that commonly fill vesicles (average 1.5 × 2.5 mm) within a phonolite dike at Wind Mountain, Otero County, New Mexico, USA. The mineral develops as tightly bound bundles (up to 0.02 × 6 mm) of acicular to bladed crystals that are elongate on [001] and flattened on the pinacoid {010}. Associated minerals include albite, aegirine, fluorapophyllite-(K), natrolite, neotocite, and montmorillonite, the last of these being observed to replace primary windmountainite. It has a dull luster, silky in aggregates, is translucent and has an orange-brown streak. It does not fluoresce under short-, medium-, or long-wave ultraviolet radiation. Windmountainite is brittle with a splintery fracture and has two good cleavages (predicted) on {110}, an estimated hardness of 2, a calculated density of 2.51 g/cm^3, and a calculated n_{avg} of 1.593. A total of $n = 30$ EMPA (WDS) analyses from six grains yielded an average of (wt.%): Na_2O 0.08, MgO 3.47, Al_2O_3 1.15, SiO_2 49.76, Cl 0.07, K_2O 0.40, CaO 0.68, TiO_2 0.30, MnO 5.64, Fe_2O_3 20.17, H_2O (calc.) 16.59, O=Cl –0.02, total 98.29. The empirical formula [based on $\Sigma(T1, T2, M2, M3) = 12$ cations *pfu*, excluding Ca, K, and Na] is: $(\square_{0.78}Ca_{0.12}K_{0.08}Na_{0.02})_{\Sigma 1.00}(Fe^{3+}_{1.93}Al_{0.04}Ti_{0.02})_{\Sigma 1.99}(Mg_{0.81}Mn^{2+}_{0.75}Fe^{3+}_{0.44})_{\Sigma 2.00}\square_2(Si_{7.81}Al_{0.17}Ti_{0.01}Fe^{3+}_{0.01})_{\Sigma 8.00}O_{20}[(OH)_{1.98}Cl_{0.02}]_{\Sigma 2.00}[(H_2O)_{3.38}(OH)_{0.62}]_{\Sigma 4.00}{\cdot}4H_2O$, yielding the simplified formula, $\square Fe^{3+}_2Mg_2\square_2Si_8O_{20}(OH)_2(H_2O)_4{\cdot}4H_2O$. The predominance of Fe^{3+} is based on color, results from the crystal-structure refinement, the crystal-chemistry of palygorskite-group minerals, the association with Fe^{3+}-dominant minerals, and considerations regarding the late-stage geochemical evolution of agpaitic rocks. The presence of H_2O and OH was determined based on results from the refined crystal structure and Fourier-transform infrared spectroscopy. Windmountainite crystallizes in the space group *C*2/*m* with *a* 13.759(3), *b* 17.911(4), *c* 5.274(1) Å, β 106.44(3)°, *V* 1246.6(1) Å^3, and $Z = 2$. The seven strongest powder X-ray diffraction lines are [*d* in Å (*I*), (*hkl*)]: 10.592 (100) (110), 5.453 (16) (130), 4.484 (19) (040), 4.173 (28) $(\bar{2}21)$, 3.319 (53) (221, 400), 2.652 (30) $(440, \bar{3}51)$, 2.530 (27) $(002, \bar{2}61)$. The crystal structure was determined from single-crystal X-ray diffraction data and refined to $R = 4.01\%$ and $wR_2 = 10.70\%$ using data from 902 reflections ($F_o > 4\sigma F_o$). It is based on sheets of inverted double chains of SiO_4 tetrahedra that sandwich ribbons of $M\varphi_6$ octahedra (φ = O, OH, H_2O, Cl), giving rise to large channels (~6.5 × 9 Å) that are occupied by loosely held H_2O groups. A modified classification of the palygorskite group [general crystal-chemical formula $M1M2_2M3_2M4_2T1_4T2_4O_{20}(OH)_2(H_2O,OH)_4{\cdot}W$] is proposed based on the occupants of the four *M* sites. Within this scheme, windmountainite is the $\square$-Fe^{3+}-Mg-$\square$ member. The palygorskite group includes six members: palygorskite (monoclinic and orthorhombic polytypes), yofortierite, tuperssuatsiaite, raite, windhoekite, and windmountainite. Windmountainite is considered to have formed from late-stage fluids that were alkaline, oxidized, and rich in both Fe^{3+} and H_2O; high aH_2O conditions are reflective of abundant, hydrated feldspathoids (natrolite and analcime) forming as primary rock-forming minerals in the phonolite at Wind Mountain.

Keywords: windmountainite, new mineral, palygorskite, crystal structure, modulated, phyllosilicate, alkaline mineralogy, nomenclature, phonolite dike, Wind Mountain, New Mexico.

§ *Corresponding author e-mail address*: dleung@laurentian.ca

Introduction

Palygorskite, $(Mg,Al)_4Si_8O_{20}(OH)_2{\cdot}8H_2O$, is a clay mineral found in epicontinental and inland basins (Akbulut & Kadir 2003, Callen 1984), carbonate soils (Verrecchia & Le Coustumer 1996), and hydrothermally altered volcanic rocks (Wang *et al*. 2009), along with alkaline igneous intrusive rocks (Chukanov *et al*. 2012). Minerals related to palygorskite are particularly diverse in alkaline igneous intrusive rocks, where several mineral species have been recorded: these include yofortierite $[(Mn^{2+},Mg,Fe^{3+},\square)_5Si_8O_{20}(OH)_2{\cdot}8H_2O$; Perrault *et al*. 1975], tuperssuatsiaite $[Na_{2-x}(Fe^{3+},Mn)_3Si_8O_{20}(OH)_2{\cdot}4H_2O$; von Knorring *et al*. 1992], raite $[Na_3Mn^{2+}{}_3Ti_{0.25}Si_8O_{20}(OH)_2{\cdot}10H_2O$; Pluth *et al*. 1997], windhoekite $[Ca_2Fe^{3+}{}_{3-x}(Si,Al)_8O_{20}(OH)_4{\cdot}10H_2O$; Chukanov *et al*. 2012], and now a new species, windmountainite.

It can be a challenge to distinguish among the distinct species related to palygorskite, owing to similarities in their morphology and appearance. In alkaline igneous intrusive rocks, all are considered to be late-stage products, typically developing as bundles or radial aggregates of acicular crystals in open vesicles. Color commonly reflects chemistry: most of the related minerals are yellow to reddish-brown as a result of Fe^{3+} enrichment (*e.g*., windhoekite and most tuperssuatsiaite). However, yofortierite (which is Mn-enriched) is typically mauve, and in rare cases, tuperssuatsiaite observed in liquid-filled vesicles can be green (Kolitsch *et al*. 2016; L. Horváth, *pers. commun*. 2020). Minerals related to palygorskite can develop as aggregates of an individual species, but multiple, related species can also occur in a single grouping (*e.g*., Chukanov *et al*. 2012). This feature, combined with the similarity in their morphology (thin, tabular to acicular) and rather complex crystal chemistry, suggests that there is a relatively high potential for new species to be discovered.

During an investigation of the rare-element mineralogy of the alkaline intrusion at Wind Mountain, New Mexico, by one of us (AMM) in 2012, specimens from a late-stage phonolite dike that cuts the main intrusion were found to contain vesicles within which acicular sprays of an unidentified orange-brown mineral were collected. The mineral resembles tuperssuatsiaite and windhoekite in terms of morphology and color, but preliminary chemical analyses indicated that it was significantly deficient in alkali elements (*i.e*., Na and Ca) relative to those minerals. This prompted a more detailed study, which has led to the recognition of this mineral as a new species: windmountainite.

To date, a comprehensive classification of palygorskite and its related minerals does not exist in the literature. At present, the *palygorskite (sub)group* is broadly considered to include minerals topologically related to palygorskite, including yofortierite, tuperssuatsiaite, and windhoekite (*e.g*., Gaines *et al*. 1997, Chukanov *et al*. 2012, Hawthorne *et al*. 2013). The general crystal-chemical formulae of these minerals can be expressed as $M1M2_2M3_2M4_2T1_4T2_4O_{20}(OH)_2(H_2O,OH)_4{\cdot}W$, where M represents octahedrally coordinated sites, T represents tetrahedrally coordinated sites, and W represents channel occupants (this study). Raite, $Na_3Mn^{2+}{}_3Ti_{0.25}Si_8O_{20}(OH)_2{\cdot}10H_2O$, is typically excluded from the group, even though it shares similar crystal-chemical features with members of the group (Pluth *et al*. 1997). The generally accepted palygorskite group designation does not adequately cover the wide range of possible chemical compositions (notably, the presence of vacancies in certain sites, *e.g*., *M*4). Throughout this contribution, the term *palygorskite-group minerals* will be used to collectively refer to these minerals, including raite, whose inclusion in the group—as will be shown—is warranted.

The crystal structures of palygorskite and sepiolite $[Mg_4Si_6O_{15}(OH)_2{\cdot}6H_2O]$ are closely related (both consist of *T-O-T* modules: in palygorskite, the *T* strips are double chains, whereas in sepiolite they are triple chains). These relationships have led to further classification schemes, including the *palygorskite-sepiolite group* (*e.g*., Guggenheim & Krekeler 2011), as well as the *palysepiole polysomatic series* (*e.g*., Ferraris & Gula 2005). The latter has been broadly linked to the biopyribole (*i.e*., biotite-pyroxene-amphibole) polysomatic series, based on the presence of homologous *T-O-T* modules that constitute all these minerals (Thompson 1978, Nespolo & Bouznari 2017).

The objectives of the present contribution are threefold: (1) to provide a complete characterization of the new mineral windmountainite, in terms of its physical, optical, chemical, and structural properties; (2) to explore the topological relationships that exist between this mineral and those related to palygorskite, leading to the formulation of a proposed hierarchal classification of the palygorskite group; and (3) to interpret the paragenesis and origin of windmountainite within the geological framework of the phonolite dike and alkaline intrusion at Wind Mountain.

Windmountainite is named after its type locality: Wind Mountain, Otero County, New Mexico, USA. The mineral and mineral name are approved by the Commission on New Minerals, Nomenclature and Classification of the International Mineralogical Association (IMA2018-130a). The holotype material has been deposited at the Canadian Museum of Nature (Gatineau, Canada), catalogue number CMNMC 87260.

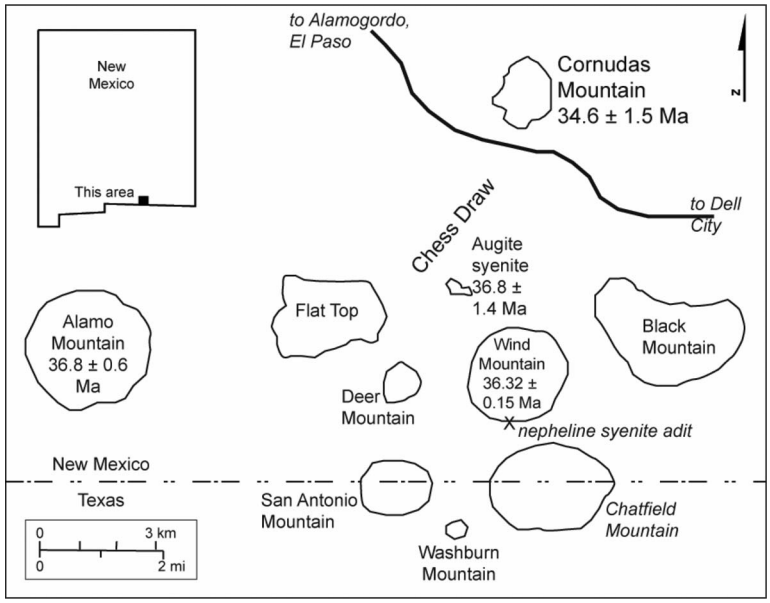

FIG. 1. Sketch map of the Cornudas Mountains (New Mexico and Texas, USA), showing the location of Wind Mountain. Age dates and errors for select intrusions are indicated. From McLemore (2018).

BACKGROUND GEOLOGY

Wind Mountain is a zoned, alkaline laccolith of Paleogene age (36.32 ± 0.15 Ma; McLemore 2018), located within the Cornudas Mountains of the Trans-Pecos Magmatic Province (McLemore *et al*. 1996; Figs. 1 and 2). The laccolith intrudes Permian carbonate rocks and is crosscut by two main, ENE-striking phonolite dikes, located on the north side of the intrusion. On average, the dikes are several meters in width, and they coalesce into one single dike at the eastern extent of the laccolith (McLemore *et al*. 1996).

Early studies of Wind Mountain and the Cornudas Mountains suggested that these intrusions were homogeneous (Zapp 1941, Timm 1941, Clabaugh 1941, Warner *et al*. 1959). Subsequent examination by McLemore *et al*. (1996) demonstrated that the Wind Mountain laccolith is actually zoned. This zonation consists of two textural varieties of nepheline syenite porphyry (core) and four types of syenite porphyry (top margin), these being interpreted as the products of crystal fractionation. While Wind Mountain is the only intrusion in the area to have been mapped in detail (*e.g*., McLemore & Guilinger 1993, McLemore *et al*. 1996), no detailed studies on the phonolite dike itself have been conducted to date. The intrusion has been evaluated as a source of raw material for glass and ceramic production (McLemore *et al*. 1996) and, more recently, has been explored for rare-element mineralization (REE + Y, Zr, Nb, Sn; Geovic Mining Corp., Denver, Colorado). For more information regarding the geology, petrology, zonation, and economic potential of Wind Mountain, the reader is directed to McLemore *et al*. (1996) and McLemore (2018).

The mineralogy of Wind Mountain is complex and includes feldspathoids (nepheline), zeolites (analcime, natrolite, chabazite-series minerals, and thomsonite-series minerals), titanosilicates (aenigmatite), zirconosilicates [catapleiite, parakeldyshite, eudialyte-group minerals, and georgechaoite (type locality)], and REE-bearing minerals (monazite-group minerals), along with aegirine, chlorite-group minerals, fluorite, microcline, olivine-group minerals, and pyrite (McLemore *et al*. 1996, Boggs 1985, Boggs & Ghose 1985, Barker & Hodges 1977). The phonolite dikes are reported to contain phenocrysts of anorthoclase (and more rarely, nepheline) and, locally, eudialyte-group minerals (McLemore *et al*. 1996, Zapp 1941, Clabaugh 1941, Warner *et al*. 1959).

OCCURRENCE

In 2012, as part of a broader study of the rare-element mineralogy of Wind Mountain (32.0314° N, 105.5042° W), Otero County, New Mexico, USA, samples of the northeastern component of the phonolite dike were collected (Fig. 3). Note that two phonolite dikes are visible on Wind Mountain, despite only one being reported (on the northeastern side of

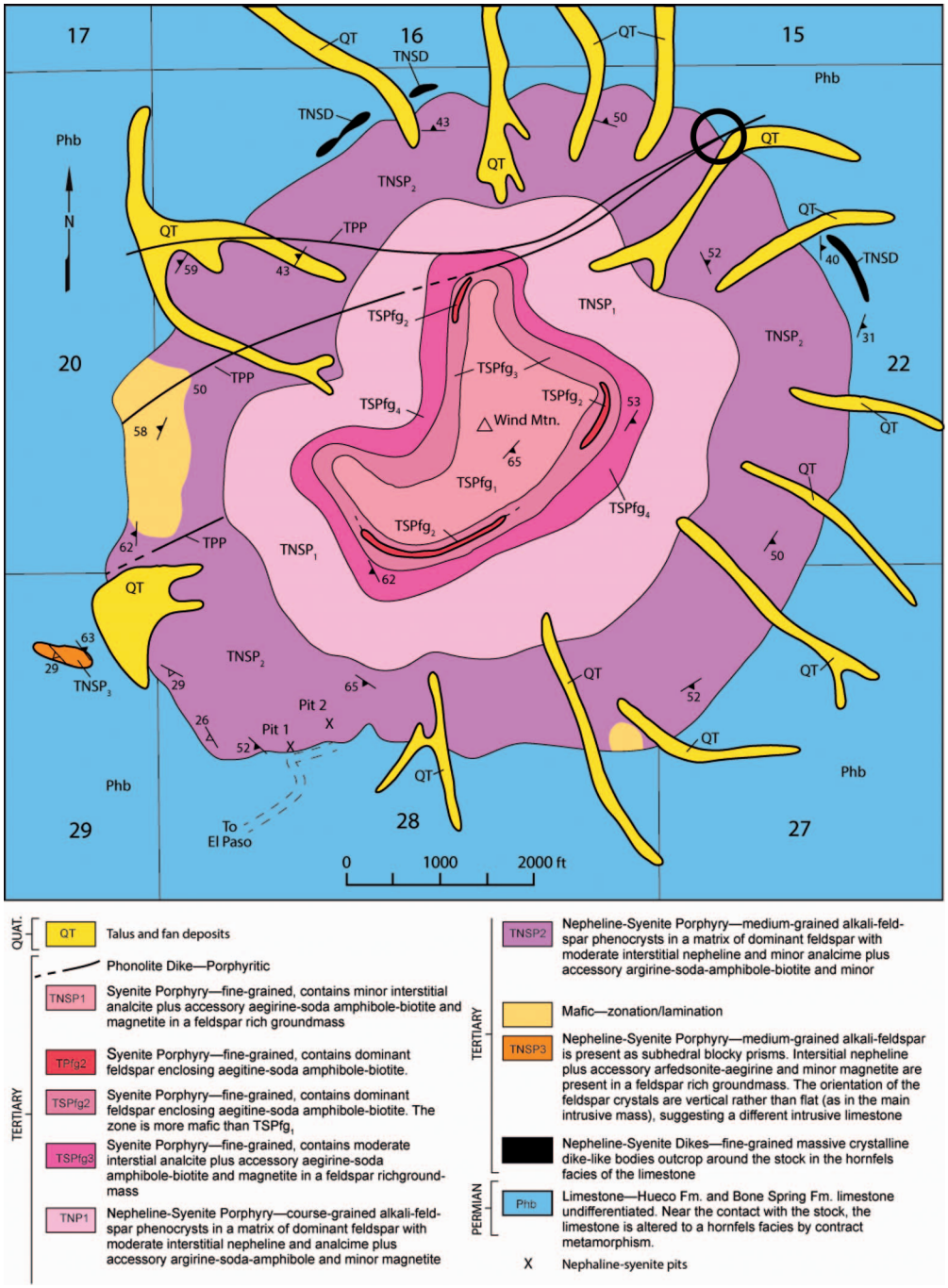

FIG. 2. Geological map of Wind Mountain. The phonolite dike (labelled TPP) in which windmountainite occurs is located on the north side of Wind Mountain and the area that was specifically sampled is denoted by a black circle. From McLemore (2018), based on field mapping by P. Graseah (July 1992).

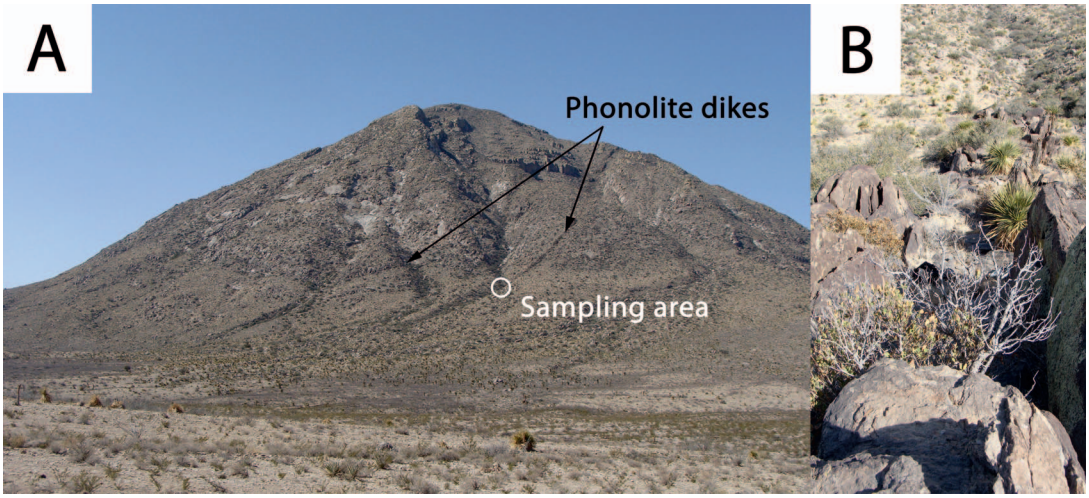

FIG. 3. (A) The northeast face of Wind Mountain (photo facing southwest), with locations of the phonolite dikes and sampling location labelled (note that the dike to the left is less prominent and appears to be unmapped on Fig. 2). (B) View of the dike looking down and northeastward; the dike is on average several meters wide.

Wind Mountain) by McLemore *et al*. (1996). The more prominent of the two dikes (presumed to be the location of main phonolite dike in Fig. 2) was sampled. The phonolite is well-exposed, dips steeply to the south (~65°), and is in sharp contact with the host intrusion. It is medium-grey in color, vesiculated (~2%, average 1.5 × 2.5 mm in diameter, up to 5 × 7 mm), and composed of alkali feldspar, analcime, albite, natrolite, aegirine, sodic amphibole, and schizolite (Grice *et al*. 2019). The vesicles, some of which contain windmountainite, commonly have bleached haloes extending to an average of 2 to 3 mm beyond the vesicle margin, but up to 8 mm for larger vesicles (Fig. 4). The minerals in or lining the walls of vesicles include: schizolite, albite, aegirine, neotocite, fluorapophyllite-(K), montmorillonite, and natrolite. These are considered to represent a secondary, later-stage assemblage developed within the phonolite.

PHYSICAL AND OPTICAL PROPERTIES

Windmountainite occurs in orange-brown to yellowish-brown, divergent, radial aggregates that typically span the entire diameter of the vesicles in which they are found (Fig. 4). The tips of aggregates tend to be reddish-brown and noticeably darker in color than the main portions of the crystals (Fig. 5A), possibly due to an elevated Mn content (based on semi-quantitative data from scanning electron microscopy–energy dispersive spectrometry, SEM-EDS). Tightly packed aggregates (up to 0.02 × 6 mm; Fig. 5B) are composed of acicular to thinly bladed crystals that are elongate on [001] and have the pinacoid {010} as the dominant form. No twinning is evident. Windmountainite has an orange-brown streak and a dull luster (silky in aggregates), is translucent, and does not fluoresce under short-, medium-, or long-wave ultraviolet radiation. The mineral has an estimated hardness of 2, a brittle tenacity, and a splintery fracture. It is predicted to have two good cleavages on {110}, based on the refined crystal structure and similarity to

FIG. 4. Hand sample of the grey phonolite with millimeter-sized vesicles containing radial aggregates of windmountainite (reddish-brown, acicular). Note the bleached haloes (white) that surround the vesicles; these extend up to 8 mm from the vesicle margin. The brown area on the right of the sample represents surface weathering.

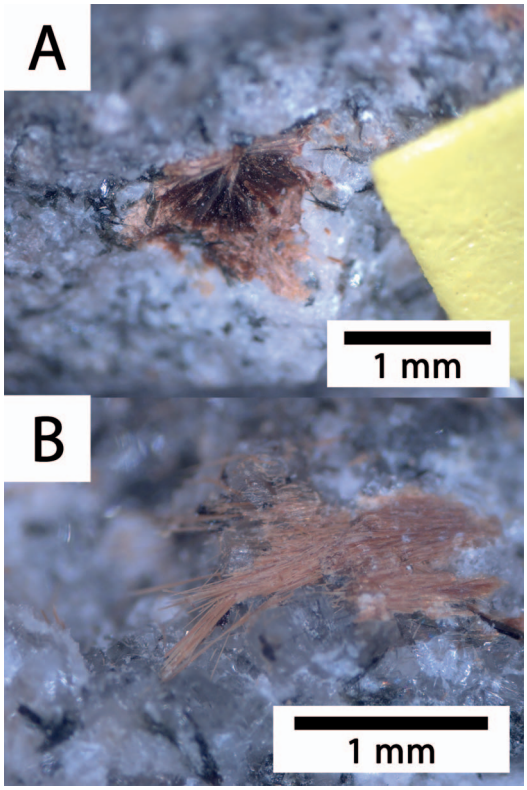

FIG. 5. (A) A radial aggregate of windmountainite showing color zoning: the cores are dark reddish-brown and the margins are lighter orange-brown (note: color zoning is only observed in aggregates). (B) Bundles of windmountainite composed of acicular to thinly bladed crystals.

amphiboles and pyroxenes. In this context, it should be noted that the literature contains inconsistencies in defining the cleavage(s) present in palygorskite-group minerals: these have been variously reported to have one or multiple, good to perfect cleavages, with the indices of the reported cleavage planes varying from species to species. Density was not measured due to the complex intergrown nature of the aggregates. The calculated density is 2.51 g/cm^3, as determined using the empirical chemical formula and refined unit-cell parameters from crystal structure analysis; this is within the reported range for palygorskite-group minerals (2.18–2.62 g/cm^3). The mineral shows no effervescence in dilute (1:10) HCl under room temperature conditions.

Optical properties could not be reliably determined owing to the small size and thinness of the examined crystals, along with the fact that they develop in complex intergrowths. Pleochroism is strong, orange-brown parallel to the length and colorless to light orange parallel to the width of crystals. Based on the recorded crystal symmetry, windmountainite is assumed to be biaxial. The average refractive index (n_{avg}), 1.593, was calculated with the program POLARIO (Fischer *et al.* 2018) using the unit-cell and positional parameters refined from single-crystal X-ray diffraction (SCXRD). The value is within the overall range of refractive indices reported for palygorskite-group minerals (1.522–1.671).

Experimental Data

Chemical analysis

Chemical analyses of windmountainite were carried out with a Cameca SX-50 electron microprobe (wavelength-dispersive spectrometry) using an accelerating voltage of 20 kV, a beam current of 10 nA, and a beam diameter of 10 μm. Ten elements were analyzed for [analyte, (X-ray line, standard)]: Na (*K*α, albite), Mg (*K*α, diopside), Al (*K*α, albite), Si (*K*α, diopside), Cl (*K*α, synthetic chlorapatite), K (*K*α, wadeite), Ca (*K*α, diopside), Ti (*K*α, synthetic $CaTiO_3$), Mn (*K*α, synthetic $MnNb_2O_6$), and Fe (*K*α, ilvaite). Samples were analyzed for F but yielded no values above detection limit. No other elements were noted in preliminary EDS scans. The H_2O content was not determined, owing to a paucity of material. It was instead calculated based on the number and multiplicity of OH and H_2O sites from the refined crystal structure: (1) an OH site of 2 *apfu*, (2) a mixed (H_2O, OH) site of 4 *apfu*, and (3) two H_2O sites totaling 4 *apfu*.

Ancillary analyses to evaluate the valence of Fe in windmountainite (*e.g.*, using Mössbauer spectroscopy, XPS, *etc.*) were not conducted owing to a paucity of material and, to a lesser extent, the degree of chemical heterogeneity. Iron is considered to be present as Fe^{3+} based on several lines of evidence: (1) a combination of SCXRD analysis and observed bond distances (*i.e.*, BVS) indicate that the valence of the species at the *M*2 site is predominantly trivalent, and as Fe is considered to be the predominant cation at this site, the implication is that Fe^{3+} is the dominant species; (2) Fe^{3+} is considered to be dominant in all Fe-bearing palygorskite-group minerals [*viz.*, tuperssuatsiaite (Cámara *et al.* 2002), palygorskite (Huang *et al.* 2007), windhoekite (Chukanov *et al.* 2012), and yofortierite (Hawthorne *et al.* 2013)], where the predominance of Fe^{3+} has been verified *via* Mössbauer spectroscopy (*e.g.*, Huang *et al.* 2007, Hawthorne *et al.* 2013); (3) the reddish-brown color of windmountainite is consistent with $Fe^{3+} > Fe^{2+}$; (4) the geochemical evolution of agpaitic rocks is associated with high and increasing fO_2 (Schönenberger & Markl 2008),

TABLE 1. SUMMARY OF KEY CHEMICAL AND CRYSTALLOGRAPHIC DATA FOR WINDMOUNTAINITE

Chemical data	
Empirical formula	$(\square_{0.78}Ca_{0.12}K_{0.08}Na_{0.02})_{\Sigma 1.00}(Fe^{3+}{}_{1.93}Al_{0.04}Ti_{0.02})_{\Sigma 1.99}$ $(Mg_{0.81}Mn^{2+}{}_{0.75}Fe^{3+}{}_{0.44})_{\Sigma 2.00}\square_2(Si_{7.81}Al_{0.17}Ti_{0.01}Fe^{3+}{}_{0.01})_{\Sigma 8.00}O_{20}$ $[(OH)_{1.98}Cl_{0.02}]_{\Sigma 2.00}[(H_2O)_{3.38}(OH)_{0.62}]_{\Sigma 4.00}\cdot 4H_2O$
Simplified formula	$(\square,Ca,K)(Fe^{3+},Al)_2(Mg,Mn^{2+},Fe^{3+})_2\square_2(Si,Al)_8O_{20}(OH)_2$ $[(H_2O),(OH)]_4\cdot 4H_2O$
Endmember formula	$\square Fe^{3+}{}_2Mg_2\square_2Si_8O_{20}(OH)_2(H_2O)_4\cdot 4H_2O$
Structural data	
Space group	*C*2/*m*
a (Å)	13.759(3)*
b (Å)	17.911(4)*
c (Å)	5.274(1)*
β (°)	106.44(3)*
V (Å^3)	1246.6(1)
Z	2

* Values refined from three-circle diffractometer data.

favoring the crystallization of Fe^{3+}-dominant species; and (5) windmountainite is associated with aegirine and neotocite [$(Mn^{2+},Fe^{3+})SiO_3\cdot H_2O$; Povondra 1996]—which are both Fe^{3+}-dominant species—suggesting that, through mineralogical association, windmountainite is also expected to be Fe^{3+}-dominant. Although no single line of evidence is unequivocal in verifying this predominance, the sum of these arguments strongly supports this interpretation. In terms of other potentially mixed-valence cations, Mn^{2+} is assumed to be predominant, based on the presence and association of windmountainite with schizolite and neotocite.

Chemical data (n = 30) from six grains of windmountainite give an average (range) of Na_2O 0.08 (*bdl*–0.18), MgO 3.47 (2.17–4.83), Al_2O_3 1.15 (0.91–1.50), SiO_2 49.76 (46.73–51.83), Cl 0.07 (*bdl*–0.12), K_2O 0.40 (0.28–0.64), CaO 0.68 (0.30–1.19), TiO_2 0.30 (0.19–0.50), MnO 5.64 (4.50–6.62), Fe_2O_3 20.17 (18.18–21.44), H_2O (calc.) 16.59, O=Cl –0.02, total 98.29 wt.%. This yields an empirical formula [based on $\Sigma(T1, T2, M2, M3) = 12$ cations *pfu*; note that *M*1 is excluded in the normalization on the basis of inferred vacancies; Table 1] of $(\square_{0.78}Ca_{0.12}K_{0.08}Na_{0.02})_{\Sigma 1.00}(Fe^{3+}{}_{1.93}Al_{0.04}Ti_{0.02})_{\Sigma 1.99}(Mg_{0.81}Mn^{2+}{}_{0.75}Fe^{3+}{}_{0.44})_{\Sigma 2.00}\square_2(Si_{7.81}Al_{0.17}Ti_{0.01}Fe^{3+}{}_{0.01})_{\Sigma 8.00}O_{20}[(OH)_{1.98}Cl_{0.02}]_{\Sigma 2.00}[(H_2O)_{3.38}(OH)_{0.62}]_{\Sigma 4.00}\cdot 4H_2O$. The endmember formula is $\square Fe^{3+}{}_2Mg_2\square_2Si_8O_{20}(OH)_2(H_2O)_4\cdot 4H_2O$, requiring Fe_2O_3 18.08, MgO 9.13, SiO_2 54.43, H_2O 18.36, total 100 wt.%.

Some grains resemble windmountainite in morphology but develop as distinctly light yellow-orange to golden sprays. Two analyses of these grains gave higher Ca contents (3.63 and 3.43 wt.% CaO; *cf* 0.68 wt.% CaO in windmountainite samples), and an average chemical formula of $(Ca_{0.60}\square_{0.29}Na_{0.07}K_{0.04})_{\Sigma 1.00}(Fe^{3+}{}_{1.96}Ti_{0.03}Al_{0.01})_{\Sigma 2.00}(Mg_{1.01}Fe^{3+}{}_{0.60}Mn_{0.39})_{\Sigma 2.00}\square_2(Si_{7.70}Al_{0.28}Ti_{0.02})_{\Sigma 8.00}O_{20}(OH_{1.98}Cl_{0.02})_{\Sigma 2.00}[(H_2O)_{2.94}(OH)_{1.06}]_{\Sigma 4.00}\cdot 4H_2O$. The relative enrichment of Ca relative to windmountainite and its depletion relative to windhoekite (*i.e*., $0.5 < Ca < 1.5$ *apfu*) suggests the mineral could be a new species, potentially the Ca-rich analogue of windmountainite.

Fourier-transform infrared spectroscopy (FTIR)

A radial aggregate of windmountainite was placed on a NaCl plate and attenuated total reflection–Fourier-transform infrared spectroscopy (ATR-FTIR) spectra were collected using a Bruker Optics Hyperion infrared microscope with an ATR objective (Ge crystal). The system was equipped with a mercury-cadmium telluride (MCT) liquid nitrogen cooled detector. The spectrum presented is a result of 100 scans in the range 4000 to 600 cm^{-1} at a resolution of 4 cm^{-1}. All spectra were corrected for contributions from atmospheric CO_2 and H_2O. Band assignments were made following those made for windhoekite (Chukanov *et al*. 2012).

The FTIR spectrum (Fig. 6) is dominated by several overlapping peaks at ~1000 cm^{-1} [914, 990, and 1103 cm^{-1}], assigned to Si–O stretching (Chukanov *et al*. 2012; see Table 2 for peak assignments). The band centered at 1191 cm^{-1} is attributed to Si–O–Si stretching vibrations associated with large (180°) bond angles; this occurs at the Si–O–Si bridge between inverted *T* ribbons and is consistent with that observed in other minerals of the palygorskite and sepiolite groups (*i.e*., the palysepiole polysomatic series; Chukanov *et al*. 2012, Tarte *et al*. 1973). The band at 662 cm^{-1} may also be derived from

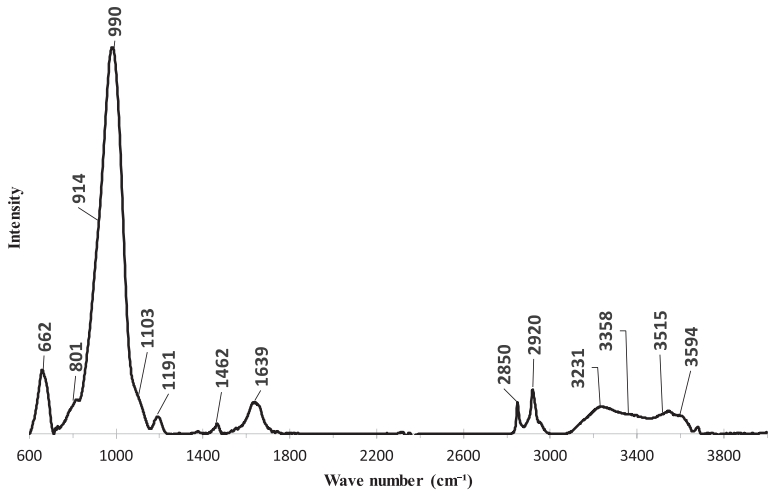

FIG. 6. ATR-FTIR spectrum of windmountainite with absorption band positions located (see Table 3 for band assignments). Peaks at 1462, 2850, and 2920 cm^{-1} are attributed to organic contamination.

the Si–O–Si bridge, but this is not unequivocal, as it could also represent an *M*–O interaction (Augsburger *et al*. 1998). The band at 1639 cm^{-1} is assigned to H_2O bending vibrations and the four bands at 3231, 3358, 3515, and 3594 cm^{-1} are assigned to O–H stretching vibrations, reflecting the four types of OH and H_2O groups that are present (OH4, OW8, OW9, and OW10). These bands are broad and diffuse, likely reflecting the relatively weak nature of the bonding with which the H_2O groups are held. Relatively weak bands are also observed at 1462, 2850, and 2920 cm^{-1}, which are unusual for silicate minerals. They are consistent with C–H bonding and may arise from trapped hydrocarbons, possibly within the relatively large channels that are present in the crystal structure; although no macroevidence exists (*e.g*., brown films overgrowing crystals), the presence of hydrocarbons has been reported in other late-stage alkaline rocks (Marks & Markl 2017).

In general, windmountainite has a similar, but distinct, FTIR spectrum to those of minerals related to palygorskite, although these distinctions are complicated by the broad nature of the peaks as a function of disorder. As noted previously, the characteristic band for palygorskite- and sepiolite-group minerals (*i.e*., the palysepiole polysomatic series) occurs at ~1190 cm^{-1} for palygorskite-group minerals and generally appears sharp, suggesting it may be useful in differentiating between these species. This band position is similar amongst several palygorskite-group minerals (windmountainite: 1191 cm^{-1}; palygorskite: 1191 cm^{-1}; yofortierite: 1196 cm^{-1}), but is at lower positions in

TABLE 2. BAND POSITIONS AND ASSIGNMENTS (FOURIER-TRANSFORM INFRARED DATA) FOR WINDMOUNTAINITE

Band position (cm^{-1})	Relative band breadth	Transmittance	Band assignment
3594	Broad	Mod. Weak	O–H stretch of H_2O
3515	Broad	Mod. Weak	"
3358	Broad	Weak	"
3231	Broad	Mod. Weak	"
1639	Moderate	Moderate	H–O–H bend
1191	Mod. Broad	Weak	Si–O–Si stretch associated with large (180°) bond angles
1103	Moderate	Mod. Weak	Si–O–Si stretch
990	Sharp	Very Strong	"
914	Moderate	Strong	"
801	Broad	Moderate	*M*–O interactions and mixed vibrations of tetrahedral layers
662	Mod. Sharp	Mod. Strong	*M*–O interactions and mixed vibrations of tetrahedral layers

others (tuperssuatsiaite: 1178 cm^{-1}; windhoekite: 1168 cm^{-1}) and therefore can be used, in broad terms, as a tool in discriminating between certain group members. However, this application is limited, particularly when resolution ($\sim$4 cm^{-1}) is considered (*i.e.*, it is not possible, in principle, to distinguish between windmountainite and palygorskite). It should be noted that, at the time of publication, the authors were unaware of an FTIR spectrum having been collected for raite, although the Raman spectrum has been reported (Ruiz-Galende *et al*. 2019). Thus, a comparison between the FTIR spectra of palygorskite-group minerals and raite cannot be made unequivocally.

Multiple attempts were made to collect a Raman spectrum of windmountainite, but none proved successful; a high background dominated the spectrum, with either no peaks or only extremely weak ones being discerned. Stability of the mineral under the laser beam ($\lambda = 532$ nm) at full or partial power does not appear to be an issue, as no obvious burn marks were noted, but the fact that no useable Raman spectrum could be obtained is intriguing. Various attempts were made to do so, including: (1) employing a different laser ($\lambda = 638$ nm); (2) collecting data from both unpolished and polished grains, along with powdered material; and (3) varying the orientation of grains with respect to the incident laser (using a Supper spindle stage). None of these attempts were successful. It is not clear why this was the case, although it may in part be related to the fibrous nature of the mineral and possibly fluorescence effects. Yofortierite was also examined by Raman spectroscopy as part of this study, using unpolished material and identical analytical conditions. This yielded a strong, well-defined pattern with sharp bands. Therefore, the reason (or reasons) why a usable Raman spectrum of windmountainite was unobtainable remains unresolved.

X-ray diffraction

Powder X-ray diffraction data were collected using a cluster of windmountainite crystals, a 114.6 mm diameter Gandolfi camera, a 0.3 mm collimator with Ni-filtered Cu$K\alpha_{avg}$ radiation ($\lambda = 1.5418$ Å), and an image plate as the detector. Both *d*-spacings and intensities were determined from a scanned image of the obtained pattern using the program DIIS (Petrus *et al*. 2012), the intensities being normalized to that of the strongest reflection, $d_{110} = 10.592$ Å. Calculated *d* and *I* values were determined using data from the refined crystal structure and the program PowderCell (Kraus & Nolze 1996), the results of which were used to determine the contribution of individual *hkl* planes to the observed reflections.

TABLE 3. POWDER X-RAY DIFFRACTION DATA FOR WINDMOUNTAINITE (THE SEVEN STRONGEST REFLECTIONS ARE GIVEN IN BOLD)

I_{obs}	I_{calc}*	d_{obs} (Å)	d_{calc} (Å)	*h*	*k*	*l*
100	**100**	**10.592**	**10.624**	**1**	**1**	**0**
16	**7**	**5.453**	**5.440**	**1**	**3**	**0**
19	**6**	**4.484**	**4.478**	**0**	**4**	**0**
28	**12**	**4.173**	**4.168**	**$\bar{2}$**	**2**	**1**
6	2	3.716	3.705	2	4	0
53	**10**	**3.319**	**3.306**	**2**	**2**	**1**
	9		**3.299**	**4**	**0**	**0**
13	6	3.271	3.272	$\bar{3}$	3	1
30	**3**	**2.652**	**2.656**	**4**	**4**	**0**
	6		**2.642**	**$\bar{3}$**	**5**	**1**
6	1	2.580	2.571	0	6	1
27	**4**	**2.530**	**2.529**	**0**	**0**	**2**
	7		**2.521**	**$\bar{2}$**	**6**	**1**
6	2	2.282	2.270	3	5	1
	1		2.263	$\bar{2}$	4	2
13	4	2.196	2.186	$\bar{4}$	6	1
8	2	2.150	2.166	2	0	2
	2		2.141	$\bar{5}$	1	2
6	1	1.621	1.616	1	11	0

*Calculated from the refined crystal structure.

Overall, the calculated and measured PXRD patterns (Table 3) show general agreement with respect to peak locations, although differences among the calculated and observed intensities are evident. The latter may, in part, be attributed to preferred orientation effects arising from the acicular habit of the material: attempts were made to randomize the grouping used, but these effects could not be eliminated. The PXRD pattern of windmountainite is dominated by a strong peak at $d_{110} = 10.592$ Å, which closely resembles that of yofortierite (10.5 Å; Perrault *et al*. 1975). The *T-O-T* modules in palygorskite-group minerals are arranged in an *en echelon* manner, when viewed on {110} (Fig. 7). Thus, the spacing corresponding to d_{110} would be expected to be, in part, related to the width and height of the *T-O-T* modules, which, in turn, would be strongly influenced by the ionic radii of the cations dominating the *M* sites that constitute the *O* layer. The cation radius not only influences the overall size of the *M* sites (larger ions resulting in expanded sites), but also directly influences the linkage of the *O* layer to the *T* layer. Therefore, the fact that the spacings corresponding to the d_{110} peaks for both windmountainite and yofortierite are nearly identical suggests that ions of similar ionic radii must occupy the *M* sites in both minerals (*i.e.*, Fe^{3+}, Mn^{2+}, Mg). Further, the spacings of the d_{110} peaks for the related minerals windhoekite and raite are both relatively larger (11.04 and 11.4 Å,

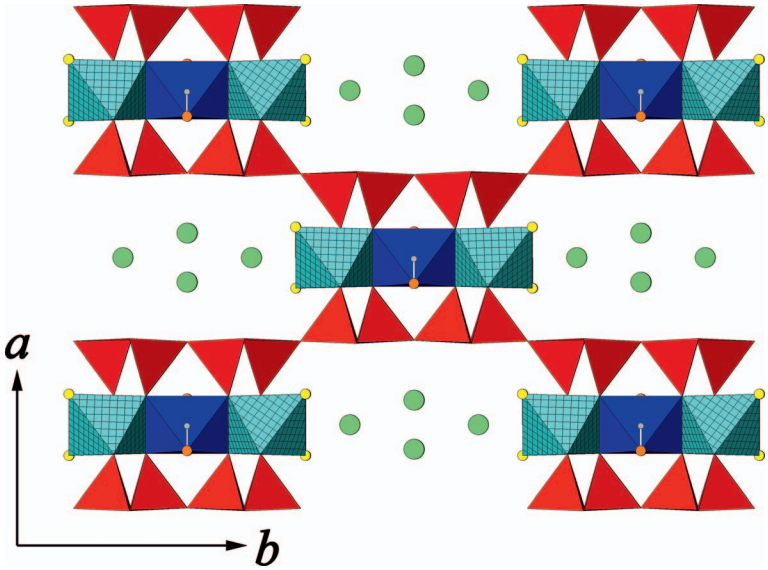

FIG. 7. The crystal structure of windmountainite projected along [001]. It shows TO_4 tetrahedra (red) that are linked to form double chains (*i.e.*, the *T* ribbon), which in turn sandwich ribbons (*O* ribbon) composed of $M\varphi_6$ octahedra (φ = O, OH, H_2O, Cl). In the *O* ribbon, $M1\varphi_6$ octahedra (dark blue, solid fill) lie at the center and are ideally vacant; $M3\varphi_6$ octahedra (cyan, cross-hatched) are located at the edge of the ribbon ($M2\varphi_6$ octahedra not pictured; see Fig. 8 for details pertaining to the *O* ribbon). This linkage produces a checkerboard-like assembly of *T*-*O*-*T* modules, the channels between which are occupied by H_2O groups (green spheres). Note the minor kinking of the *T* ribbons from planarity.

respectively; Perrault *et al*. 1975, Pushcharovskii *et al*. 1999), principally owing to the *M* sites being occupied by cations with larger radii (*e.g*., Ca and Na) and, to a lesser extent, the inclusion of an additional, partially occupied, *M* site (see section on topological relationships of palygorskite-group minerals for further discussion).

Isolating a single crystal for single-crystal X-ray diffraction (SCXRD) analysis was problematic, given the fine-grained nature of the mineral. Therefore, a data set for SCXRD was obtained using a small grouping of windmountainite crystals, but one where the individual grains were sufficiently lined up such that only a small, discrete, offset-diffraction component was noted. The grouping gave a reasonably sharp (but not ideal) extinction under cross-polarized light. The diffraction-spot shapes obtained from this aggregate were not uniform in all directions, but at the same time did not exhibit the directional streaking typically associated with disorder. This implies that the analyzed group exhibits a high level of crystallographic continuity and, in general, that the mineral is reasonably well-ordered. The grouping was attached to a tapered glass fiber and mounted on a Bruker *D*8 three-circle diffractometer equipped with a rotating-anode generator (Mo$K\alpha$ radiation), an APEX-II CCD area detector, and a fixed detector-to-crystal distance of 5 cm. Intensity data were collected to 50.23° 2θ using frame widths (ω) of 0.5° and exposure times of 120 s per frame. An empirical absorption correction was applied (SADABS; Sheldrick 2008), and the data were corrected for Lorentz, polarization, and background effects. All reflection data were then merged using the program XPREP ver. 5.1 (Bruker AXS, USA). Information relevant to the data collection and crystal-structure determination of windmountainite is given in Table 4.

The SHELXL-97 program package (Sheldrick 1997, 2015), available through the Oscail environment (McArdle *et al*. 2004), was used to solve and refine the crystal structure. Results gave $|E^2 - 1| = 1.063$, suggesting the presence of a center of symmetry. The space group $C2/m$ was selected based on several lines of evidence: (1) there were no violations of the extinction conditions for a *C*-centered lattice; (2) a relatively high number of exceptions ($n = 264$) were noted for a possible *c*-glide; (3) the Laue ($2/m$) merging was 5.17%, suggesting monoclinic symmetry; and (4) most of the minerals related to palygorskite crystallize in the space group $C2/m$ (Cámara *et al*. 2002, Chukanov *et al*. 2012, Hawthorne *et al*. 2013). An *E*-map was produced from which the positions of Si, Fe, Mg, and most O atoms were located. Through subsequent difference Fourier maps, the rest of the O

TABLE 4. DATA COLLECTION AND CRYSTAL-STRUCTURE REFINEMENT DETAILS FOR WINDMOUNTAINITE

Data collection	
Instrument	Bruker *D*8 diffractometer
Crystal size (μm)	7 × 13 × 75
μ (Mo*K*α)	3.13 mm^{-1}
Average temperature (*K*)	293
Detector to sample distance (mm)	50
Omega increment (°)	0.5
Exposure per frame (s)	120
2θ limit (°)	50.23
Total collected reflections	4430
Unique reflections	1158
Unique observed $\|F_o\| \geq 4\sigma_F$	902
$R_{int.}$	0.0367
R_σ	0.0297
hkl range	$-16 \leq h \leq 16$; $-21 \leq k \leq 21$; $-6 \leq l \leq 6$
Refinement	
Reflection file type	HKL
R_1 ($F_o > 4\sigma F_o$)	0.0401
R_1 (all data)	0.0586
wR_2	0.1070
S = *GooF*	1.136

sites, as well as sites assigned to Ca and H, were located. Cation-site assignments were made on the basis of site scattering, bond distances, and chemical data, whereas anion site assignments were made on the basis of bond-valence sum (BVS) calculations from the refined crystal structure (using reference data from Brese & O'Keeffe 1991).

The final structure of windmountainite was refined to $R = 4.01\%$ and $wR_2 = 10.70\%$ with anisotropic displacement factors for all atoms except H. Table 5 contains the final positional and equivalent isotropic and anisotropic displacement factors for all atoms. Table 6 contains selected interatomic distances. Table 7 contains assigned site populations, along with observed *versus* calculated bond distances for the *M* sites. Table 8 contains BVS data.

Crystal Structure Description

The T sites

The *T* sites (*T*1 and *T*2) have average bond distances of 1.619 and 1.617 Å, respectively (Table 6), close to the ideal Si–O bond distance of 1.62(1) Å (Smith & Bailey 1963). These near-ideal values suggest a high-degree of Si ordering and minimal substitution of Si by other cations (*e.g.*, Al, Ti, Fe^{3+}, *etc.*). The latter is aligned with results of the chemical data and calculation of the empirical formula, which give a combined (*T*1, *T*2) site assignment of $(Si_{7.81}Al_{0.17}Ti_{0.01}Fe^{3+}_{0.01})_{\Sigma 8.00}$ *apfu*. The average bond distance calculated using this cation-site assignment and data from Shannon (1976) is 1.623 Å, which is close to ideal and consistent with those determined for the *T*1 and *T*2 sites.

The M sites

There are three distinct octahedrally coordinated sites in the crystal structure: *M*1, *M*2, and *M*3 (Table 5). The *M*1 site has an average bond distance of 2.180 Å and represents the largest of the three *M* sites (Table 6). Given the non-trivial presence of alkali and alkaline-earth elements and the size of this site, Ca, K, and Na were apportioned here. Site assignment from the empirical formula is $(\square_{0.78}Ca_{0.12}K_{0.08}Na_{0.02})_{\Sigma 1.00}$ *apfu*, indicating the site is dominated by vacancies. Assuming Ca at the *M*1 site gives a refined site-occupancy factor of 0.310(9) and a corresponding effective site scattering of 6.2(2) *epfu*. This is similar to the value of 4.1 *epfu*, calculated from the site assignment (Table 7) and confirms the site is vacancy dominant. The average observed *M*1–O bond distance is 2.180 Å, which differs from the calculated bond distance (based on site assignments) of 2.502 Å (Table 7). Such a difference is not considered significant, given the vacancy-dominant nature of the *M*1 site.

The *M*2 site has the shortest average *M*–O bond distance (2.013 Å) of the three *M* sites (Table 6). Assuming it to be occupied by Fe gives a refined site occupancy factor of 0.927(5), corresponding to $(Fe_{1.85}\square_{0.15})_{\Sigma 2.00}$ *apfu*. Data from the empirical formula suggest a site assignment of $(Fe^{3+}_{1.93}Al_{0.04}Ti_{0.02})_{\Sigma 1.99}$ *apfu*. This yields an effective site scattering of 51.4 *epfu*, which is consistent with that calculated from the refined data [48.2(3) *epfu*; Table 7]. Site refinement indicates a formal charge of 2.803 and site assignments indicate an average charge of 3.01 (Table 7); both thus infer a formal charge of ~3+ for the site. The observed bond distance of 2.013 Å (Table 7) agrees well with the calculated bond distance of 2.002 Å from the site assignment.

The *M*3 site was considered to have a mixed (Mn + Mg) composition for refinement purposes only, given the chemical data and the fact it is not possible to distinguish between Mn and Fe owing to the similarity in their X-ray scattering curves. The refined site-occupancy factors for *M*3 are Mn 0.76(1) and Mg 0.24(1), corresponding to an occupancy of $(Mn_{1.52}Mg_{0.48})_{\Sigma 2.00}$ *apfu*. These indicate a composition of Mn > Mg; however, Mn and Fe cannot be distinguished

TABLE 5. POSITIONAL AND DISPLACEMENT PARAMETERS (Å^2) FOR WINDMOUNTAINITE

Atom	Refined Site Occupancy	*x*	*y*	*z*	U^{11}	U^{22}	U^{33}	U^{23}	U^{13}	U^{12}	U^{eq}/U^{iso}
*M*1	Ca 0.310(9)	½	½	½	0.018(4)	0.021(4)	0.011(4)	0	0.008(3)	0	0.016(2)
*M*2	Fe 0.927(5)	½	0.41482(5)	0	0.0218(7)	0.0148(6)	0.0058(6)	0	0.0043(5)	0	0.0141(4)
*M*3	Mn 0.76(1) Mg 0.24(1)	½	0.32016(6)	½	0.0242(8)	0.0219(7)	0.0057(7)	0	0.0025(5)	0	0.0176(5)
*T*1		0.29185(1)	0.41475(6)	–0.4735(3)	0.0218(8)	0.0137(6)	0.0075(7)	–0.0005(5)	0.0052(6)	–0.0008(5)	0.0141(4)
*T*2		0.2911(1)	0.33414(7)	0.0234(3)	0.0240(8)	0.0133(7)	0.0067(7)	–0.0003(5)	0.0052(6)	–0.0019(5)	0.0145(4)
O1		¼	¼	0	0.035(3)	0.015(2)	0.021(3)	–0.002(2)	0.009(2)	–0.007(2)	0.023(1)
O2		0.2519(4)	½	–0.4983(9)	0.028(3)	0.017(2)	0.017(3)	0	0.005(2)	0	0.021(1)
O3		0.4126(3)	0.3382(2)	0.1123(6)	0.025(2)	0.018(2)	0.012(2)	0.002(1)	0.008(1)	–0.001(1)	0.0180(8)
OH4		0.4223(4)	½	0.094(1)	0.021(3)	0.017(2)	0.024(3)	0	0.013(2)	0	0.019(1)
O5		0.4138(3)	0.4088(2)	–0.3779(6)	0.026(2)	0.020(2)	0.009(2)	–0.001(1)	0.004(1)	0.001(1)	0.0189(8)
O6		0.2462(2)	0.3765(2)	–0.7604(6)	0.026(2)	0.022(2)	0.009(2)	–0.005(1)	0.005(1)	–0.002(1)	0.0191(8)
O7		0.2430(2)	0.3730(2)	–0.2643(6)	0.027(2)	0.022(2)	0.009(2)	0.004(1)	0.005(1)	–0.001(1)	0.0194(8)
OW8		0.4080(4)	0.2393(3)	0.5942(9)	0.058(3)	0.056(3)	0.030(3)	–0.004(2)	0.010(2)	–0.010(2)	0.049(1)
OW9		0.426(1)	0	1.200(3)	0.16(1)	0.12(1)	0.23(2)	0	0.13(1)	0	0.156(6)
OW10		½	0.1415(6)	1	0.073(6)	0.128(9)	0.083(7)	0	0.005(5)	0	0.098(3)
H4		0.4966(4)	½	0.15(2)							0.08(3)

TABLE 6. OBSERVED BOND DISTANCES (Å) FOR WINDMOUNTAINITE

*T*1–O5	1.614(4)
*T*1–O2	1.616(2)
*T*1–O6	1.617(3)
*T*1–O7	1.628(3)
<*T*1–O>	1.619
*T*2–O1	1.602(1)
*T*2–O3	1.605(4)
*T*2–O6	1.630(3)
*T*2–O7	1.630(3)
<*T*2–O>	1.617
*M*1–OH4 ×2	2.105(5)
*M*1–O5 ×4	2.218(3)
<*M*1–O>	2.180
*M*2–OH4 ×2	2.004(3)
*M*2–O5 ×2	2.013(3)
*M*2–O3 ×2	2.021(3)
<*M*2–O>	2.013
*M*3–OW8 ×2	2.074(5)
*M*3–O3 ×2	2.083(3)
*M*3–O5 ×2	2.185(3)
<*M*3–O>	2.114

due to their similar scattering powers, so the potential for Fe also occupying the site is high, based on the abundance of Fe from the chemical data. Thus, the proportions of Mg, Mn, and Fe were constrained to agree with those from the chemical data. These yield a site assignment of $(Mg_{0.81}Mn^{2+}_{0.75}Fe^{3+}_{0.44})_{\Sigma 2.00}$ *apfu* and a calculated site scattering of 39.9 *epfu*, in agreement with that determined from the refined data [45.3(5) *epfu*; Table 7]. The calculated bond distance from the site assignment (2.104 Å; Table 7) is consistent with the average observed bond distance of 2.114 Å. Bond-valence calculations from the site refinement indicate a formal charge of 2.383 (Table 8); this is consistent with that derived from site assignments (2.22; Table 7). These support the site being predominantly occupied by R^{2+} cations, with a lesser, but significant, R^{3+} occupancy. On this basis, the *M*3 site was assigned an ideal occupancy of Mg_2 *apfu*. However, the range of chemical variation in the *M*3 site is considerable, with site compositions showing a range of $(Mg_{1.10–0.54}Mn_{0.86–0.63}Fe^{3+}_{0.77–0.15})_{\Sigma 2.00–1.98}$. The site assignments based on the crystal-structure refinement suggest that the dominant cation at the *M*3 site is Mg ($n = 18$), although some show it is Mn^{2+} ($n = 9$), and fewer showing that it is Fe^{3+} ($n = 3$). The high degree of chemical variability at the *M*3 site raises the potential for yet-to-be-discovered Mn^{2+}- and Fe^{3+}-analogues of windmountainite.

TABLE 7. ASSIGNED SITE POPULATIONS AND OBSERVED *VERSUS* CALCULATED BOND DISTANCES (BASED ON DATA FROM SHANNON 1976) FOR *M* SITES IN WINDMOUNTAINITE

Site	Site scattering (*epfu*)		Average bond distance (Å)		Site population (*apfu*)		Formal charge	
	Refined	Effective	Observed	Calculated	Refined	Assigned	Refined	Assigned
*M*1	6.2(2)	4.1	2.180	2.502	0.69 □ + 0.31 Ca	0.78 □ + 0.12 Ca + 0.08 K + 0.02 Na	1.056	0.34
*M*2	48.2(3)	51.4	2.013	2.002	1.85 Fe^{3+} + 0.15 □	1.93 Fe^{3+} + 0.04 Al + 0.02 Ti	2.803	3.01
*M*3	45.3(5)	39.9	2.114	2.104	1.52 Mn^{2+} + 0.48 Mg	0.81 Mg + 0.75 Mn^{2+} + 0.44 Fe^{3+}	2.383	2.22

TABLE 8. CALCULATED BOND VALENCE SUMS (BVS) FOR WINDMOUNTAINITE

	*M*1	*M*2	*M*3	*T*1	*T*2	H4	Anion Σ
O1	-	-	-	-	1.061 $^{x2\rightarrow}$	-	2.122
O2	-	-	-	1.022 $^{x2\rightarrow}$	-	-	2.044
O3	-	0.457 $^{x2\downarrow}$	0.428 $^{x2\downarrow}$	-	1.053	-	1.938
OH4	0.214 $^{x2\downarrow}$	0.478 $^{x2\rightarrow\downarrow}$	-	-	-	0.922	2.092*
O5	0.157 $^{x4\downarrow}$	0.466 $^{x2\downarrow}$	0.325 $^{x2\downarrow}$	1.027	-	-	1.976
O6	-	-	-	1.019	0.984	-	2.003
O7	-	-	-	0.989	0.984	-	1.973
OW8	-	-	0.438 $^{x2\downarrow}$	-	-	-	0.438
OW9	-	-	-	-	-	-	0
OW10	-	-	-	-	-	-	0
Cation Σ	1.056	2.803	2.383	4.057	4.082	0.922	

* Includes the contribution from H4.

Anion sites

Anion sites were determined to be dominated by O, OH, or H_2O using calculated BVS values from the refined crystal structure (Table 8). Results show that the majority of anions at the anion sites are O, with several exceptions: (1) OH4, which has a BVS of 1.170 eV, suggesting it is OH; (2) OW8, which has a BVS of 0.438 eV, indicating it is an H_2O group with potential OH substitution; and (3) OW9 and OW10, which have BVS values of 0 eV, indicating that both represent H_2O groups. Only one H position, that associated with the OH4 site, could be located from the difference Fourier map; this has a BVS contribution of 0.922 eV, resulting in a total BVS of 2.092 eV for OH4. The OH4 site has a site composition of $[(OH)_{1.98}Cl_{0.02}]_{\Sigma 2.00}$ *apfu* based on results from the crystal-structure refinement and chemical analyses. The OW9 and OW10 sites are both associated with high U_{eq} values [0.156(6) and 0.098(3), respectively], indicating a high degree of disorder, a feature consistent with loosely bound H_2O groups. The site assignment for the OW8 site is $[(H_2O)_{3.38}(OH)_{0.62}]_{\Sigma 4.00}$ *apfu*, whereas the total site assignment for the OW9 and OW10 sites is $4H_2O$ *apfu*.

Crystal structure

The crystal structure of windmountainite consists of *T*-*O*-*T* modules elongated along [001] (Fig. 7). The *T* ribbons are composed of SiO_4 tetrahedra linked into double chains, with the apices of the tetrahedra pointing towards the *O* ribbons, these being sandwiched between pairs of *T* ribbons. This produces a T^+-*O*-T^- configuration, where + and − denote the relative direction of the apex of a tetrahedron along [100]. The *T* ribbons are not strictly planar but rather are slightly bent, as evidenced by the slight variations in the *x* coordinates of *T* sites (Table 5). The *O* ribbons consist of a honeycomb strip of three edge-sharing $M\varphi_6$ octahedra (φ = O, OH, H_2O, Cl; *M*1 and *M*3) that alternate with two edge-sharing $M2\varphi_6$ octahedra along [001] (Fig. 8). In windmountainite, the centers of the honeycomb strips (*i.e.*, *M*1 sites) are dominantly vacant. Based on the *x* coordinates of the *M* sites (Table 5), the *O* ribbon is planar.

The *T*-*O*-*T* modules are cross-linked *via* T^+–T^- and T^-–T^+ bonds, forming a checkerboard of *T*-*O*-*T* modules that give rise to large channel spaces (~6.5 × 9 Å) when viewed along [001] (Fig. 7). Since the SiO_4 double chains are linked to those of adjacent *T*-*O*-*T* modules, a continuous plane of linked SiO_4 tetrahedra is developed along [001] and [010], but with the tetrahedra ($n = 4$) being inverted along [010]. The T^+–T^- and T^-–T^+ bonds result in large *T*2–*O*1–*T*2 bond angles [180.00(3)°] where the double-chains are cross-linked; this is atypical for most silicate minerals. The other three Si–O–Si bond angles [141.9(3)°, 136.7(2)°, and 133.7(2)°] are typical of minerals based on *T*-*O*-*T* modules such as mica-group and amphibole-supergroup minerals (ideally ~141°, calculated based on the trigonometry of planar six-membered SiO_4 rings that are present in chains and sheets), with slight deviations due to the non-planar nature of the *T* ribbons.

A hydroxyl group (OH4) is joined to $M1\varphi_6$ and $M2\varphi_6$ octahedra. It is located within the center of ring-like structures within the SiO_4 double chains, similar to that observed in minerals of the amphibole supergroup and mica group (Hawthorne *et al*. 2012, Hendricks & Jefferson 1939). A structurally bound H_2O group (OW8) is bound to *M*3 at the sides of the *O* ribbon, where there is no bonding available with the *T* ribbon; a similar feature is observed in sepiolite-group minerals (*e.g.*, Guggenheim & Krekeler 2011). Two loosely bound H_2O groups (OW9 and OW10) reside in the channels between the *T*-*O*-*T* modules.

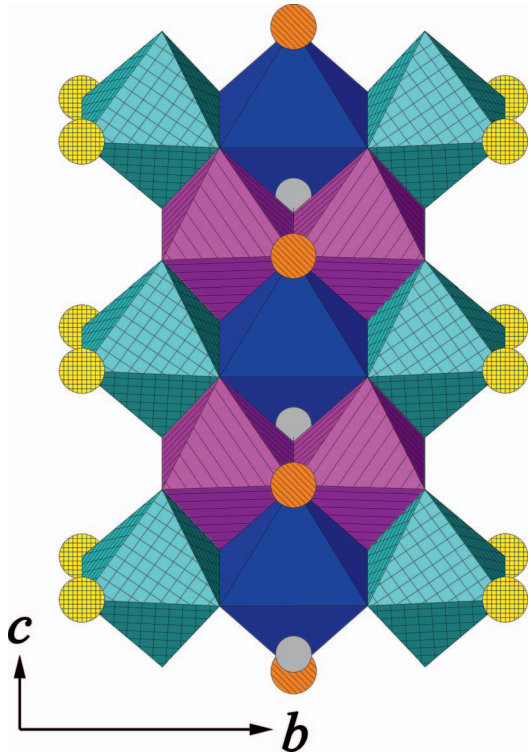

FIG. 8. The *O* ribbon of windmountainite projected along [100]. The $M\varphi_6$ octahedra ($\varphi = O, OH, H_2O, Cl$) are: $M1\varphi_6$ (dark blue, solid fill), $M2\varphi_6$ (fuchsia, line-hatched), and $M3\varphi_6$ (cyan, cross-hatched). The OH and structurally bound H_2O groups are represented by spheres: OH4 (orange, line-hatched; bonded to H4, grey sphere, solid fill), and OW8 (yellow, cross-hatched).

TOPOLOGICAL RELATIONSHIPS

Structural relationship to other minerals

The PXRD pattern of windmountainite strongly resembles those of minerals related to palygorskite, suggesting these minerals share considerable crystal-structure similarities. Bradley (1940) first solved the accepted structure of palygorskite (this being based on *T-O-T* modules of double-chain width, linked by T^+ and T^- bonds) in the space group *C*2/*m* using material from Attapulgus, Georgia, USA. Artioli & Galli (1994) refined the crystal structures of both orthorhombic (*Pbmn*) and monoclinic (*C*2/*m*) polytypes of palygorskite in a sample from Bolca, Italy. Several new mineral species related to palygorskite have been described, all of which have been shown to crystallize in the monoclinic crystal system (space group *C*2/*m*) based on SCXRD (Cámara *et al*. 2002, Chukanov *et al*. 2012, Hawthorne *et al*. 2013). It should be noted that a comprehensive crystal-chemical classification scheme applicable to palygorskite-group minerals does not exist, meaning that detailed comparisons between windmountainite and palygorskite-group minerals cannot be made in a straightforward manner. In this context, development of such a classification is deemed essential, as it provides the basis and opportunity to clearly define the intra- and interrelationships among these minerals.

In general, the crystal structures of palygorskite-group minerals all consist of *T-O-T* modules elongated on [001] (Fig. 7). The *T* ribbons are composed of SiO_4 tetrahedra linked into double chains, with the apices of the tetrahedra pointing towards to the sandwiched *O* ribbon between the *T* ribbons. The *T-O-T* strips are linked by T^+-T^- and T^--T^+ bonds along [010], yielding corrugated sheets of inverted double chains of SiO_4 tetrahedra, which extend along [010] and [001] (Fig. 7). The $M\varphi_6$ octahedra are arranged in honeycomb ribbons oriented along [001], sandwiched between double chains of SiO_4 tetrahedra (Bradley 1940; Fig. 8). When viewed along [001], the *T-O-T* ribbon modules form a checkerboard pattern with large channels that are occupied by loosely bound H_2O (Fig. 7). The crystal structure of windmountainite, as presented previously, is clearly consistent with those

of palygorskite-group minerals (see Table 9 for comparative data between minerals of the palygorskite group).

The *T* ribbon includes two *T* sites (*T*1, *T*2) that are predominantly occupied by Si, although minor substitution of Al, Ti, and Fe^{3+} may be possible. The *T* sites generally show low distortion and are close to ideal for tetrahedrally coordinated sites (see Table 10 for calculated polyhedral data for the *T* sites in palygorskite-group minerals). However, the *T* ribbon itself exhibits a range in concavity: (1) flat in tuperssuatsiaite; (2) slightly bent in palygorskite, windmountainite, and yofortierite; and (3) concave in windhoekite and raite (Cámara *et al*. 2002, Post & Heaney 2008, this study, Chukanov *et al*. 2012, Hawthorne *et al*. 2013, Pluth *et al*. 1997). In general, the concavity of the *T* ribbon is directly related to the structural size mismatch between the *T* and *O* ribbons, and, in particular, the size of ions which occupy the *M*3 site, as the site is linked to both *T* sites. A perfectly planar arrangement involving the *T* and *O* ribbons (*i.e*., having no concavity), considering an average *T*–O bond distance of 1.619 Å (the average for *T* sites among all palygorskite-group minerals) and assuming no distortion in the *O* ribbon, requires an average calculated *M*–O bond distance of 2.159 Å. Assuming an ideal ionic radius for O^{2-} of 1.36 Å (Shannon 1976), the *M* cation is then required to have an ideal radius of 0.799 Å. In situations where cations occupying the *M*3 site are smaller than this radius, the width of the *O* ribbon is relatively constricted, resulting in the $T2O_4$ tetrahedra rotating toward the center of the *T*-*O*-*T* module, thus causing the *T* ribbon to bend in a slightly convex manner. Conversely, when the *M* cations are of a larger radius, the *O* ribbon expands in width along [100], causing the $T2O_4$ tetrahedra to rotate away from the center of the *T*-*O*-*T* module, thus forcing the *T* ribbon to bend in a concave manner. In this sense then, the range in concavity observed in the *T* ribbon among palygorskite-group minerals is directly related to the radii of the cations occupying the *M*3 site. Palygorskite, which shows the least concavity in the *T* ribbon, has an average *M*3–O bond distance of 2.086 Å (see Table 10 for calculated polyhedral data for the *M* sites of palygorskite-group minerals). The concavity increases in moving from windmountainite (2.114 Å) to yofortierite (2.183 Å) to windhoekite (2.240 Å) and finally to raite (2.401 Å), which exhibits the greatest concavity. Note that although the size of the *M*3 site in yofortierite (2.183 Å) is greater than that expected for planarity (2.159 Å), and that this would be predicted to yield a concave *T* ribbon, the *T* ribbon is actually marginally bent, likely owing to the variability of bond lengths among different *T* and *M* sites. Moreover, an exception to this trend also occurs in tuperssuatsiaite, where the average ionic radius of cations in the *M*3 site is substantially larger (2.406 Å), but the *T* ribbon has a flat, rather than concave, geometry. This can be explained as the structural mismatch being accommodated by horizontal distortion of the *M*3 site, instead of through distortion of the *T* ribbon. The *M*3 site is significantly distorted in tuperssuatsiaite compared to other palygorskite-group minerals: the average distortion index (Baur 1974) of the *M*3 site in tuperssuatsiaite is 0.051 (Table 10), which is the greatest among all three *M* sites in all palygorskite-group minerals (average 0.023). Additionally, the bond angle variance of the *M*3 site in tuperssuatsiaite (256.319°^{2}; Table 10) is also the greatest for the three sites among all palygorskite-group minerals (average 59.842°^{2}). The elevated distortion of the *M*3 site coincides with a reduction in the number of channel H_2O *apfu*, possibly due to structurally bound H_2O (OW8) shifting into the channel to compensate for the high degree of horizontal distortion.

The *O* ribbon consists of four octahedrally coordinated *M* sites: *M*1, *M*2, *M*3, *M*4 (Fig. 9). The *M*1, *M*2, and *M*3 sites form regular edge-sharing octahedra, which share vertices with the TO_4 tetrahedra of the double chains in the *T* ribbons from above and below. The *M*1, *M*2, and *M*3 sites can be occupied by a variety of cations (see next section), and bond distances combined with refined site scattering results suggest that cation ordering occurs within the different *M* sites.

Vacancies are common in the *M*1, *M*2, and *M*3 sites of palygorskite-group minerals as a function of their complex chemistry and modular crystal structures. Notably, the *M*1 site can be dominated by vacancies, as in windmountainite and palygorskite, which results in an intermediate, dioctahedral-trioctahedral-like *O* ribbon (*e.g*., Chryssikos *et al*. 2009). Moreover, endmember compositions of some palygorskite-group minerals require vacancies for local charge-balance considerations: tuperssuatsiaite has vacancies at the *M*3 site and windhoekite has vacancies at the *M*2 and *M*3 sites (Cámara *et al*. 2002, Chukanov *et al*. 2012).

The *M*4 site is the most unusual among the four *M* sites present in palygorskite-group minerals, as it is either vacancy-dominated or only partially occupied (<50%). The latter is observed in windhoekite (~40% occupancy; Chukanov *et al*. 2012) and raite (~13–45% occupancy; the estimated range is based on both chemical data and structure refinement from Pluth *et al*. 1997). The *M*4 site is positioned at the edge of the *T*-*O*-*T* module, leading to the potential development of two bonds with the $T2O_4$ tetrahedra and up to four bonds with H_2O groups. Both windhoekite and raite contain an additional channel H_2O group (relative to other palygorskite-group minerals), leading to devel-

TABLE 9. COMPARATIVE DATA FOR PALYGORSKITE-GROUP MINERALS

	Windmountainite	Palygorskite*	Yofortierite	Tuperssuatsiaite	Windhoekite	Raite
Chemical formula	$\square Fe^{3+}{}_2Mg_2\square_2Si_8O_{20}(OH)_2(H_2O)_4{\cdot}4H_2O$	$\square Al_2Mg_2\square_2Si_8O_{20}(OH)_2(H_2O)_4{\cdot}4H_2O$	$MnMn_2Mn_2\square_2Si_8O_{20}(OH)_2(H_2O)_4{\cdot}4H_2O$	$Fe^{3+}Fe^{3+}{}_2(Na,\square)_2\square_2Si_8O_{20}(OH)_2(H_2O)_4{\cdot}2H_2O$	$Fe^{3+}(Fe^{3+},\square)_2(Ca,\square)_2(\square,Ca)_2Si_8O_{20}(OH)_2(H_2O,OH)_4{\cdot}6H_2O$	$Mn^{2+}Mn^{2+}{}_2Na_2(\square,Ti)_2Si_8O_{20}(OH)_2(H_2O)_4{\cdot}Na(H_2O)_6$
Crystal system	Monoclinic	Monoclinic	Monoclinic	Monoclinic	Monoclinic	Monoclinic
Space group	*C*2/*m*	*C*2/*m*	*C*2/*m*	*C*2/*m*	*C*2/*m*	*C*2/*m*
Unit cell						
a	13.759(3)	12.681(3)	14.169(1)	14.034(7)	14.319(5)	15.1(1)
b	17.911(4)	17.864(9)	17.858(2)	17.841(7)	17.825(4)	17.6(1)
c (Å)	5.274(1)	5.127(3)	5.2919(5)	5.265(2)	5.242(1)	5.290(4)
β (°)	106.44(3)	92.23(5)	105.878(1)	103.67(4)	103.5(2)	100.5(2)
V (Å^3)	1246.6(1)	1160.6(7)	1287.9(3)	1280.9(9)	1301.0(6)	1382.33
Z	2	2	2	2	2	2
ρ (g/cm^3)	2.51 (calc.)	2.35 (calc.)	2.18	2.28 (calc.)	2.62(2)	2.39(2)
Optical data						
Average R.I.	1.593 (calc.)					
α	*n.d.*	1.522–1.528	1.530	1.5388(5)	1.610(3)	1.540(2)
β	*n.d.*	1.530–1.546	*n.d.*	1.5596(5)	1.662(3)	1.542(2)
γ	*n.d.*	1.533–1.548	1.559	1.595(1)	1.671(3)	1.550(2)
2*V* (°)	*n.d.*	30–61	*n.d.*	104(2)	50(10)	53 (calc.)
Strongest XRD lines: [*I* (%), *d* (Å), (*hkl*)]	100, 10.592, (110) 16, 5.453, (130) 19, 4.484, (040) 28, 4.173, ($\bar{2}$21) 53, 3.319, (221, 400) 30, 2.652, (440, $\bar{3}$51) 27, 2.530, (002, $\bar{2}$61)	100, 10.35, (110) 19, 6.33, (200) 29, 4.462, (040) 16, 3.223, (31$\bar{1}$) 23, 3.170, (400) 17, 2.536, (061)	100, 10.5, (110) 18, 4.41, (021) 15, 3.68, ($\bar{2}$21) 90, 3.302, ($\bar{3}$01) 30, 2.621, ($\bar{4}$21) 15, 2.526 (510) 20, 2.510 (002)	100, 10.82, (110) 20, 4.140, (021) 30, 3.395, (131) 40, 2.638 (510) 30, 2.544, (44$\bar{1}$) 30, 2.510, (170) 30, 2.235, (13$\bar{2}$)	100, 11.04, (110) 10, 4.432, (021, 111) 6, 4.134, (22$\bar{1}$, 31$\bar{1}$) 11, 3.486, (400, 221) 8, 2.636, (35$\bar{1}$, 11$\bar{2}$) 6, 2.507 (26$\bar{1}$)	100, 11.351, (110) 12, 4.460, (021) 9, 4.142 ($\bar{2}$21) 14, 2.925 (510) 22, 2.639 (35$\bar{1}$)
References	This study	Anthony *et al.* (2001), Christ *et al.* (1969).	Hawthorne *et al.* (2013), Perrault *et al.* (1975)	Anthony *et al.* (2001), Cámara *et al.* (2002), von Knorring *et al.* (1992), Karup- Møller & Petersen (1984)	Chukanov *et al.* (2012)	Pluth *et al.* (1997), Pushcharovskii *et al.* (1999), Mer'kov *et al.* (1973), Anthony *et al.* (2001), this study

* Monoclinic polytype
n.d. = not determined

TABLE 10. CALCULATED POLYHEDRAL DATA FOR *M* SITES OF PALYGORSKITE-GROUP MINERALS USING VESTA (MOMMA & IZUMI 2008)

	Windmountainite	Palygorskite	Yofortierite	Tuperssuatsiaite	Windhoekite	Raite
*T*1						
Average bond length (Å)	1.619	1.622	1.621	1.615	1.619	1.624
Polyhedral volume (Å^3)	2.171	2.187	2.182	2.156	2.172	2.190
Distortion index (bond length)	0.003	0.012	0.004	0.002	0.007	0.008
Quadratic elongation	1.001	1.001	1.001	1.001	1.002	1.003
Bond angle variance (°^{2})	5.652	2.303	5.592	5.596	4.518	12.228
Effective coordination number	3.999	3.963	3.996	4.000	3.990	3.988
*T*2						
Average bond length (Å)	1.617	1.624	1.617	1.610	1.619	1.621
Polyhedral volume (Å^3)	2.164	2.183	2.162	2.134	2.168	2.173
Distortion index (bond length)	0.008	0.004	0.013	0.011	0.006	0.013
Quadratic elongation	1.001	1.004	1.002	1.002	1.003	1.004
Bond angle variance (°^{2})	5.324	15.747	8.575	8.579	10.911	16.559
Effective coordination number	3.991	3.997	3.977	3.978	3.993	3.975
*M*1						
Average bond length (Å)	2.180	2.158	2.147	2.064	2.022	2.073
Polyhedral volume (Å^3)	13.486	12.393	13.002	11.528	10.900	11.810
Distortion index (bond length)	0.023	0.025	0.021	0.022	0.029	0.025
Quadratic elongation	1.018	1.054	1.010	1.012	1.009	1.005
Bond angle variance (°^{2})	52.899	170.457	30.645	36.217	22.920	11.229
Effective coordination number	5.846	5.818	5.873	5.857	5.738	5.820
*M*2						
Average bond length (Å)	2.013	1.873	2.079	2.037	2.055	2.155
Polyhedral volume (Å^3)	10.781	8.578	11.872	11.098	11.390	13.073
Distortion index (bond length)	0.003	0.027	0.007	0.021	0.011	0.013
Quadratic elongation	1.006	1.015	1.006	1.011	1.011	1.014
Bond angle variance (°^{2})	19.717	50.959	19.745	35.314	35.396	47.776
Effective coordination number	5.998	5.796	5.990	5.874	5.963	5.950
*M*3						
Average bond length (Å)	2.114	2.086	2.183	2.406	2.240	2.401
Polyhedral volume (Å^3)	12.396	11.806	13.636	16.689	14.647	17.735
Distortion index (bond length)	0.022	0.028	0.025	0.051	0.030	0.021
Quadratic elongation	1.012	1.018	1.012	1.077	1.017	1.027
Bond angle variance (°^{2})	38.343	59.003	39.823	256.319	55.548	94.840
Effective coordination number	5.880	5.714	5.842	5.365	5.715	5.881
*M*4						
Average bond length (Å)	-	-	-	-	2.309	2.291
Polyhedral volume (Å^3)	-	-	-	-	12.753	14.909
Distortion index (bond length)	-	-	-	-	0.046	0.135
Quadratic elongation	-	-	-	-	1.186	1.071
Bond angle variance (°^{2})	-	-	-	-	442.969	93.898
Effective coordination number	-	-	-	-	5.349	2.037
Reference	This study	Post & Heaney (2008)	Hawthorne *et al.* (2013)	Cámara *et al.* (2002)	Chukanov *et al.* (2012)	Pluth *et al.* (1997)

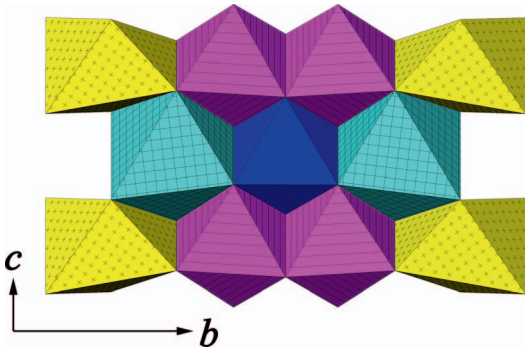

FIG. 9. The *O* ribbon in raite (Pluth *et al*. 1997) projected along [100], consists of $M1\varphi_6$ (dark blue, solid fill; $\varphi = O$, OH, H_2O, Cl), $M2\varphi_6$ (fuchsia, line-hatched), $M3\varphi_6$ (cyan, cross-hatched), and $M4\varphi_6$ octahedra (yellow, marked with +). Note that the *M*4 site is dominantly vacant in all palygorskite-group minerals; the $M4\varphi_6$ octahedra are only shown for discussion purposes. The highly distorted nature of the *M*4 site is due to irregular bonds that would be made with H_2O groups residing in the channels between *T*-*O*-*T* modules.

opment of a $^{[6]}M4$ site, rather than the $^{[5]}M4$ site as seen in other palygorskite-group minerals. Partial occupancy of the *M*4 site in windhoekite and raite may be the result of local charge-balance requirements: for minerals with vacant *M*4 sites (*viz*., palygorskite, yofortierite, tuperssuatsiaite, and windmountainite), the effective charge arising from the four *M* sites is 10+, whereas it departs from this value for minerals with partially occupied *M*4 sites, *viz*., windhoekite (12+) and raite (8+). The distortion index of the *M*4 site in windhoekite is greater than the average for the *M*1, *M*2, and *M*3 sites (0.046 *versus* 0.023; Table 10), with that in raite being significantly greater (0.135; Table 10), these clearly demonstrating the highly distorted nature of the site. The *M*4 site in palygorskite-group minerals is reminiscent of the *B* (*i.e*., *M*4) site in amphibole-supergroup minerals; however, while it is vacancy dominant in palygorskite-group minerals, it is generally occupied by cations in amphibole-supergroup minerals (Hawthorne *et al*. 2012).

The channels between *T*-*O*-*T* modules along [001] are typically occupied by loosely bound H_2O. The number of channel H_2O groups *pfu* in palygorskite and related minerals is variable: tuperssuatsiaite ideally contains 2 *apfu* of channel H_2O; palygorskite, yofortierite, and windmountainite contain 4 *apfu*; and windhoekite and raite contain 6 *apfu* of channel H_2O. Typically, the channel H_2O groups are loosely bound and highly disordered, based on the relatively high thermal displacement parameters of the O atoms associated with the groups (~0.04–0.9 $Å^2$; this study, Cámara *et al*. 2002, Chukanov *et al*. 2012, Hawthorne *et al*. 2013, Pluth *et al*. 1997). However, as noted previously, some channel H_2O groups are partially bound to the *M*4 site in both windhoekite and raite. Raite has channels occupied by $Na(H_2O)_6$ octahedra (Pluth *et al*. 1997), which is unique among minerals related to palygorskite. Moreover, the *T* modules in raite also exhibit the greatest degree of concavity. Such concavity would increase the channel space, which would in turn facilitate occupancy of the channel by larger cations (*e.g*., Na) in addition to H_2O. The presence and size of these channels contribute to palygorskite having important industrial applications. For example, they can accommodate more complex compounds, such as indigo (*i.e*., Maya Blue; Chiari *et al*. 2003), raising the potential for varied occupants, natural or anthropogenic, within the channels. Moreover, the presence of H_2O and/or alkali elements in channels of palygorskite and related minerals is reminiscent of that observed in other layered silicates (*e.g*., smectite and illite; Bailey 1980) and framework silicates such as zeolites (Coombs *et al*. 1997).

The question of whether H_2O plays an essential role in palygorskite and related minerals is key to understanding their crystal-chemical variability, their stability, and the conditions under which they can develop. Palygorskite-group minerals all contain appreciable H_2O contents. Using values extracted from the existing literature (von Knorring *et al*. 1992, Karup-Møller & Petersen 1984, this study, Perrault *et al*. 1975, Hawthorne *et al*. 2013, Mer'kov *et al*. 1973, Bradley 1940, Chukanov *et al*. 2012), the concentration of H_2O ranges from tuperssuatsiaite (9.77–11.39 wt.%), to windmountainite (16.59 wt.%), to yofortierite (16.69–17.22 wt.%), to raite (19.37 wt.%), to palygorskite (19.86–20.01 wt.%), and to windhoekite (21.0 wt.%). The observed ranges in H_2O content include both structurally bound OH groups (2 *apfu*) and H_2O groups (4 *apfu*), as well as channel H_2O groups, the latter ranging from 2–6 *apfu*. In their study into the dehydration character of palygorskite, Post & Heaney (2008) found that the loss of structural H_2O (OW8) occurs in two stages over the range 475–725 K. Dehydration over increasing temperature results in a concomitant folding of the *T*-*O*-*T* modules and the loss of the 180° bond angles of the Si–O–Si bridges between *T*-*O*-*T* modules. As noted previously, the 180° bond angles result from the T^+–T^- and T^-–T^+ bonds which serve to link adjacent *T*-*O*-*T* modules and are key crystal-structure features of minerals belonging to the palysepiole polysomatic series. The implication, then, is that the presence of structurally bound H_2O (as opposed to loosely held channel H_2O) is essential to

these minerals, primarily because of the fact it stabilizes the structural integrity of the bridges between *T*-*O*-*T* modules. As the H_2O contents of palygorskite-group minerals are appreciable, *i.e.*, 9.77 to 21.0 wt.%, the implication is that conditions of high aH_2O are essential to their formation. Furthermore, the variability in channel H_2O present in palygorskite-group minerals suggests that a relationship exists, at least in part, between individual species and their requirements of specific aH_2O conditions.

Proposed classification

A comprehensive, IMA-sanctioned classification scheme for palygorskite-group minerals does not currently exist, although several implicit classifications have been proposed (*e.g.*, Gaines *et al*. 1997, Strunz & Nickel 2001, Chukanov *et al*. 2012, Guggenheim & Krekeler 2011). Within the Dana classification scheme (Gaines *et al*. 1997), windmountainite is classified as 74 phyllosilicate modulated layers, 74.03 with joined strips, 74.03.01 palygorskite-sepiolite group, 74.03.01a palygorskite subgroup, 74.03.01a.04 windmountainite. Within the Nickel-Strunz classification scheme (Strunz & Nickel 2001), it is classified as 9 silicates, 9.E phyllosilicates, 9.EE single tetrahedral nets of 6-membered rings, 9.EE.20 windmountainite (also palygorskite, yofortierite, and tuperssuatsiaite).

In general, these schemes broadly consider the general chemistry of these related minerals, but they do not take into account the crystal-chemical features that are known, *e.g.*, several crystallographically distinct *M* and *T* sites exist and can be occupied by a variety of cations. A general crystal-chemical formula for palygorskite-group minerals has not been proposed, likely owing to the crystal-chemical complexity of the palygorskite group, coupled with the challenges associated with analyzing them (Chukanov *et al*. 2012). Ferraris & Gula (2005) provide a crystal-structure classification of the palygorskite and sepiolite groups (*i.e.*, the palysepiole polysomatic series) but do not discuss the classification of minerals within the palygorskite group. Furthermore, isolated attempts have been made at distinguishing between members of the group on the basis of the dominant occupants of the *M*1, *M*2, and *M*3 sites, but these have been insufficiently developed so as to provide a classification scheme for palygorskite-group minerals (*e.g.*, Chukanov *et al*. 2012, Hawthorne *et al*. 2013). It is therefore necessary to explicitly propose a classification scheme for the palygorskite group in order to better understand the crystal-chemical relationships that exist among palygorskite-group minerals, although the classification scheme presented herein is not meant to be an exhaustive overview of the crystal chemistry of the group.

Palygorskite-group minerals are almost all monoclinic in symmetry, the only exception being orthorhombic palygorskite (Artioli & Galli 1994). It should be noted that these minerals have modulated crystal structures based on homologous *T*-*O*-*T* modules reminiscent of amphibole-supergroup minerals and mica-group minerals. Therefore, any differences in symmetry that might be observed would be attributed to stacking variations, and thus the minerals resulting from these variations would have to be considered polytypes, rather than distinct mineral species (Bailey *et al*. 1977). As such, the polytypes of palygorskite should be more properly designated as palygorskite-*Mabc* and palygorskite-*Oabc*.

In considering the general crystal-structure features common to palygorskite-group minerals, a general structural formula is proposed as follows:

$$M1M2_2M3_2M4_2T1_4T2_4O_{20}(OH)_2(H_2O,OH)_4{\cdot}W$$

The important constituents present in the various sites, based on known mineral species and reported chemical data, are given as follows:

$M1 = Fe^{3+}$, □, Mn^{2+}, Ca, Mg;
$M2 = Fe^{3+}$, Mn^{2+}, Al, □;
$M3$ = Mg, Na, Mn^{2+}, Ca, Fe^{3+}, □;
$M4$ = □, Ca, Ti^{4+}, Mn^{2+};
$T1$ = Si, Al, Ti^{4+}, Fe^{3+};
$T2$ = Si, Al, Ti^{4+}, Fe^{3+};
$W = nH_2O$, $Na(H_2O)_6$

It should be noted that the *M*4 site is included in this formula, although it is largely vacant in palygorskite-group minerals. However, as discussed earlier, this site can be partially occupied and may be required to satisfy local charge-balance requirements. It must be remembered that *W* represents channel occupants and that these do not, strictly speaking, occupy unique sites; rather, it is taken to represent the sum or aggregate of many potential sites in the channel, in order to account for the variable concentrations of H_2O that may be present in these minerals.

Applying this general structural formula to palygorskite (*sensu stricto*) yields $M1 = □$, $M2$ = Al, $M3$ = Mg, $M4 = □$, and $T1$, $T2$ = Si, with $W = 4H_2O$, *i.e.*, palygorskite would be considered as the □-Al-Mg-□ member of the palygorskite group, based on occupancies of the *M*1-*M*2-*M*3-*M*4 sites. By the same token, windmountainite has the following site occupancies: $M1 = □$, $M2 = Fe^{3+}$, $M3$ = Mg, $M4 = □$, and $T1$, $T2$ = Si, with $W = 4H_2O$ and thus represents the □-Fe^{3+}-Mg-□ member. This approach can be extended to the remaining members of the palygorskite group, and the

TABLE 11. CLASSIFICATION SCHEME FOR PALYGORSKITE-GROUP MINERALS
$[M1M2_2M3_2M4_2T1_4T2_4O_{20}(OH)_2(H_2O,OH)_4 \cdot W]$

Mineral	Sites (and site coordinates)							References
	*M*1 (½, ½, ½)	*M*2 (½, *y*, 0)	*M*3 (½, *y*, ½)	*M*4 (½, *y*, 0)	*T*1 (*x*, *y*, *z*)	*T*2 (*x*, *y*, *z*)	*W*	
Windmountainite	□	Fe^{3+}	Mg	□	Si	Si	$4H_2O$	This study
Palygorskite	□	Al	Mg	□	Si	Si	$4H_2O$	Post & Heaney (2008)
Yofortierite	Mn^{2+}	Mn^{2+}	Mn^{2+}	□	Si	Si	$4H_2O$	Hawthorne *et al.* (2013)
Tuperssuatsiaite	Fe^{3+}	Fe^{3+}	Na, □	□	Si	Si	$2H_2O$	Cámara *et al.* (2002)
Windhoekite	Fe^{3+}	Fe^{3+}, □	Ca, □	□, Ca	Si	Si	$6H_2O$*	Chukanov *et al.* (2012)
Raite	Mn^{2+}	Mn^{2+}	Na	□, Ti	Si	Si	$Na(H_2O)_6$	Pluth *et al.* (1997)

□, *x* indicates a vacancy-dominated site with partial occupancy by cation *x*, as required for charge-balance considerations of endmember formulae.
x, □ indicates a cation-dominated site with partial vacancies, as required for charge-balance considerations of endmember formulae.
* The extra $(OH)_2$ *apfu* in windhoekite, from data of Chukanov *et al.* (2012), is probably located at the OW8 $[(H_2O,OH)_4]$ structural site.

classification and respective ordering schemes of the palygorskite group are tabulated in Table 11. The *M*4 site is dominantly vacant but its presence must be acknowledged: in some minerals (windhoekite and raite), a partially occupied *M*4 site is required to achieve a charge-balanced endmember formula.

In previous literature (*e.g.*, Post & Heaney 2008), endmember palygorskite [$Mg_2Al_2Si_8O_{20}(OH)_2 \cdot 8H_2O$, *sensu stricto*] was found to have the following *M* site occupancies: *M*1 = □, *M*2 = Al, *M*3 = Mg, *M*4 = □. The ionic radii of Al and Mg are quite similar (0.535 Å *versus* 0.72 Å, respectively; Shannon 1976) and this may partially explain why the mineral exhibits considerable $2Al^{3+} \leftrightarrow 3Mg^{2+}$ substitution (Suárez & García-Romero 2011). Despite this, an Mg-dominant analogue of palygorskite has not yet been described, which is curious given that most palygorskite develops in Mg-rich environments (*e.g.*, dolomite-rich sediments and basins). Such a mineral would have an endmember composition of $Mg_5Si_8O_{20}(OH)_2 \cdot 8H_2O$ and would require >3.5 Mg *apfu*. An examination of the chemical data for palygorskite in the literature (*e.g.*, Suárez & García-Romero 2011) shows that most analyses give ≤3.5 Mg *apfu*, *i.e.*, the minerals corresponding to these are in fact palygorskite, *sensu stricto*. These data may suggest the existence of a crystal-chemical barrier limiting the extent of Mg incorporation into palygorskite, *i.e.*, there may be a crystal-chemical threshold to the incorporation of Mg in palygorskite. At the same time, there is a limited set of chemical data in the literature that suggests the possible existence of a Mg-dominant analogue of palygorskite (*e.g.*, Chukanov *et al.* 2012), which potentially challenges this hypothesis. Clearly, there is much room for further research on the matter.

The palygorskite group classification proposed herein should also include raite [$Na_3Mn^{2+}{}_3Ti_{0.25}Si_8O_{20}(OH)_2 \cdot 10H_2O$; Pluth *et al.* 1997], a mineral typically excluded from those designated as belonging to the palygorskite group (*e.g.*, Ferraris & Gula 2005, Hawthorne *et al.* 2013, Pluth *et al.* 1997, Cámara *et al.* 2002, Chukanov *et al.* 2012). This exclusion appears to stem principally from the presence of a $[Na(H_2O)_6]$ complex residing in the channel, rather than the typical, loosely bound, H_2O groups that characterize palygorskite-group minerals. The $[Na(H_2O)_6]$ complex technically occupies an *M* site (which shares edges with *M*4), the product of which results in a quasi-continuous *O* layer in raite. This feature is unlike that in any other member of the palygorskite group, wherein only discrete *O* ribbons are present. However, the vacancy-dominated nature of the *M*4 site (~13–45% occupancy; Pluth *et al.* 1997) suggests that the $[Na(H_2O)_6]$ complex is not strictly joined to the *O* ribbon and should, instead, be considered as a channel occupant (Pluth *et al.* 1997). In this sense, raite should be considered a member of the palygorskite group, with $W = Na(H_2O)_6$ in the general crystal-chemical formula, and its formula rewritten as $Mn^{2+}Mn^{2+}{}_2Na_2(□,Ti)_2Si_8O_{20}(OH)_2(H_2O)_4 \cdot Na(H_2O)_6$ (Table 9).

Further evidence of the relationship of raite to members of the palygorskite group is present in the PXRD data. While the calculated PXRD pattern for raite (Table 12) resembles that of the palygorskite-group minerals, the experimental pattern (ICDD reference pattern 00-025-1318, Mer'kov *et al.* 1973) differs substantially. The lack of internal agreement

TABLE 12. POWDER X-RAY DIFFRACTION DATA FOR RAITE FROM THE LOVOZERO MASSIF, KOLA PENINSULA, RUSSIA (THE FIVE STRONGEST REFLECTIONS ARE GIVEN IN BOLD)

I_{obs}	I_{calc}*	d_{obs} (Å)	d_{calc} (Å)	h	k	l
100	**100**	**11.3508**	**11.3485**	**1**	**1**	**0**
4	3	8.8709	8.8000	0	2	0
3	5	5.6873	5.6742	2	2	0
4	2	5.4274	5.4562	1	3	0
12	**10**	**4.4599**	**4.4778**	**0**	**2**	**1**
4	3	4.4039	4.4000	0	4	0
9	**5**	**4.1421**	**4.1316**	**2**	**2**	**$\bar{1}$**
2	2	3.7802	3.7851	2	4	0
3	7	3.7076	3.7118	4	0	0
1	3	3.6389	3.6449	1	3	1
5	2	3.5765	3.5930	2	2	1
3	1	3.4208	3.4200	4	2	0
1	2	3.3342	3.3593	0	4	1
3	1	3.2947	3.2847	3	3	$\bar{1}$
3	2	3.2149	3.2055	2	4	$\bar{1}$
2	2	3.1159	3.1071	4	2	$\bar{1}$
14	**9**	**2.9248**	**2.9280**	**5**	**1**	**0**
4	2	2.8099	2.8069	1	5	1
22	**15**	**2.6394**	**2.6321**	**3**	**5**	**$\bar{1}$**
4	2	2.5991	2.6001	0	0	2
2	1	2.5493	2.5550	0	6	1
5	1	2.5002	2.4998	2	2	$\bar{2}$
5	4	2.4874	2.4854	2	6	$\bar{1}$
7	5	2.4581	2.4614	1	1	2
3	1	2.4055	2.4066	3	5	1
3	2	2.3488	2.3565	4	4	1
3	1	2.3156	2.3258	2	0	2
2	1	2.2568	2.2611	4	2	$\bar{2}$
4	1	2.2060	2.2118	1	7	1
2	1	2.1895	2.1954	5	5	$\bar{1}$
8	1	2.1207	2.1147	6	4	$\bar{1}$
2	1	2.0931	2.0877	7	1	$\bar{1}$
3	1	2.0693	2.0658	4	4	$\bar{2}$
4	3	2.0202	2.0218	4	6	1
1	1	1.9936	1.9995	3	7	1
1	1	1.9778	1.9821	6	0	$\bar{2}$
2	1	1.9538	1.9680	4	0	2
2	1	1.8480	1.8628	6	6	$\bar{1}$
1	1	1.8300	1.8187	3	9	0
2	1	1.8048	1.8050	7	5	$\bar{1}$
2	1	1.7646	1.7600	0	10	0
2	2	1.7174	1.7120	8	4	$\bar{1}$
2	1	1.6828	1.6814	2	8	$\bar{2}$
2	2	1.6443	1.6489	6	0	2
3	2	1.6357	1.6374	7	5	1
1	1	1.6161	1.6131	0	4	3
2	1	1.5923	1.5908	1	11	0
3	1	1.5713	1.5738	1	5	$\bar{3}$
2	1	1.5597	1.5585	3	5	$\bar{3}$
3	1	1.5412	1.5440	6	4	2
4	1	1.5121	1.5187	9	1	$\bar{2}$
1	1	1.4756	1.4667	0	12	0
2	2	1.4438	1.4415	8	6	1
1	1	1.4387	1.4377	7	9	0
2	1	1.4177	1.4189	3	5	3
2	1	1.4060	1.4034	2	10	2
1	2	1.3725	1.3767	9	5	1
2	1	1.3453	1.3454	1	11	2
2	1	1.3021	1.3036	4	0	$\bar{4}$
2	1	1.2845	1.2860	5	11	$\bar{2}$
3	1	1.2801	1.2775	0	12	2

*Calculated from Pluth *et al.* (1997).

between the calculated and observed patterns for raite may be attributed to a combination of poor crystallinity and the techniques used to collect the data. To investigate this, a new pattern was collected using material from the Lovozero Massif, Kola Peninsula, Russia [see Table 12 for the experimental PXRD pattern of raite, along with the calculated pattern using data from Pluth *et al.* (1997)]. Powder X-ray diffraction data for raite were collected with a Bruker D8 microdiffractometer operated at 40 mA and 40 kV, using Cu$K\alpha_{avg}$ radiation ($\lambda = 1.5418$ Å), a Hi-Star 2-D area detector and a sample-to-detector distance of 16.0 cm. A grouping of fibers was mounted on a glass filament and rotated about the ϕ axis to maximize grain randomization. Data were collected over a range of 5 to 95° 2θ using a frame width of 10° and a counting time of 4 h per frame. This new experimental pattern is considered more complete with more precisely determined intensity values and is consistent with the pattern calculated from the refined crystal structure (Pluth *et al.* 1997). Results confirm the strongest line occurs at $d_{110} = 11.351$ Å, similar to the ~10.5 Å line characteristic of all palygorskite-group minerals. Moreover, two other strong reflections ($d_{021} = 4.460$ and $d_{22\text{-}1} = 4.142$ Å) are shared by at least three other palygorskite-group minerals. Among the palygorskite-group minerals, the observed PXRD pattern of raite most closely resembles that of windhoekite. As noted earlier, both are relatively unique within the palygorskite group because they have partially occupied *M*4 sites. This relationship suggests that subtle crystal-structure features of minerals in the palygorskite group may be evident in their PXRD patterns. It is further noteworthy that the PXRD patterns of windmountainite, tuperssuatsiaite, and palygorskite contain a major peak at $d_{040} = 4.460$–4.484 Å, and those of palygorskite, windmountainite,

and windhoekite contain a major peak at $d_{400} = 3.170$–3.486 Å, both of which are absent from the PXRD pattern for raite. The reason for these discrepancies is unknown.

The complex crystal-chemistry of palygorskite-group minerals, combined with the fact that multiple species can occur together, suggests that the true diversity of the palygorskite group is considerably more significant than the limited number of species recorded to date. Several examples of potentially new members of the palygorskite group include the Mg-endmember of palygorskite (*e.g.*, Chukanov *et al.* 2012), along with Ca-, Fe-, and Mn-analogues of windmountainite as presented in this contribution. However, these potential members have been considered solely on the basis of chemical data, and confirmation of these species will require structure refinement *via* SCXRD or allied data (*e.g.*, Rietveld analysis of PXRD data). However, obtaining usable XRD data on palygorskite-group minerals is commonly problematic because these minerals typically form as poorly developed, acicular to thinly bladed crystals. Synchrotron-based XRD techniques show promise in solving the structures of potential palygorskite-group minerals, due to the higher X-ray flux—and therefore, better signal-to-noise ratios—of synchrotron data (Pluth *et al.* 1997). On the whole, any future discoveries within the palygorskite group will help to better elucidate the intra- and interrelationships between members of the palygorskite group and the conditions under which they develop.

Genetic Implications

Although several studies have documented the general mineralogy and petrology of Wind Mountain (*c.f.* McLemore 2018), none have focused on the late-stage phonolite dikes, so little is known of them. As such, a preliminary study of the geological and mineralogical characteristics of the phonolite dike has been undertaken herein, so as to generalize its geological and mineralogical features and to elucidate its role with respect to the formation of windmountainite. This study is not intended to be comprehensive in scope, but rather, presents a general overview, based on relatively limited observations and their subsequent conclusions. It is based on hand-sample observations (gross textures, mineralogy), along with analyses from optical petrography (grain sizes, textures, minerals present), SEM-EDS (quantitative mineral chemistry), and whole-rock PXRD (mineral identification, combined with Rietveld refinement for modal abundances). No detailed whole-rock major-element, trace-element, or allied analyses were made and the data presented is limited to samples obtained from the lowermost ~30 m of the exposed part of the northeastern-most portion of the phonolite dike.

Mineralogical, textural, and petrographic analysis of the phonolite dike

The primary (rock-forming) and secondary (vesicle) mineralogy of the phonolite dike was initially determined through optical microscopy and SEM-EDS. These aided in mineral identification, along with providing data on textural relationships and mineral chemistry, all of which were integrated into a proposed mineral paragenetic sequence for the phonolite dike.

In hand sample, the phonolite is grey with a vitreous to waxy luster on fresh surfaces and is reddish-brown with a dull luster on weathered surfaces (Fig. 4). Disseminated vesicles (~2 modal %; dimensions ranging from 1.5 × 2.5 mm up to 5 × 7 mm) are found throughout, these characteristically displaying distinctly bleached haloes (Fig. 4). Rare euhedral phenocrysts (<1 modal %, up to ~5 mm) of annite, aegirine, alkali feldspar, and an unidentified dark-red mineral occur in an equigranular, fine-grained groundmass. The unidentified dark-red mineral is prismatic and, in some cases, develops as tubular-like crystals with a conchoidal-like fracture and no obvious cleavage. Results from preliminary Raman spectroscopic analyses suggest it may be a mica or a batisite-group mineral, but further study is necessary to confirm its identity.

Examination of a polished thin section of the phonolite using plane- and cross-polarized transmitted light (Fig. 10) reveals that the phonolite is equigranular with pilotaxitic domains of alkali feldspar and analcime. The alkali feldspar and analcime are spatially associated with one another and commonly display strong pitting when viewed under high magnification by SEM. Crystals of subhedral to anhedral natrolite (average 200 × 300 μm, up to 300 × 500 μm) are colorless, developing in blocky, clot-like aggregates (Fig. 10). Backscattered electron images reveal sharp contacts between natrolite and analcime (Fig. 11), consistent with an overgrowth (or contemporaneous growth) relationship, rather than involving alteration. Aegirine and sodic amphibole are disseminated throughout the sample, forming as euhedral to subhedral (interstitial) crystals. Backscattered-electron images also show aegirine to be zoned with respect to Zr, the concentration of which increases from core to rim, consistent with an increase in incompatible elements during magma evolution. While the increase in Zr content is clear, no concomitant changes in Na, Ca, Fe, Si, or Al content, were noted. Interestingly, the changes in Zr content are

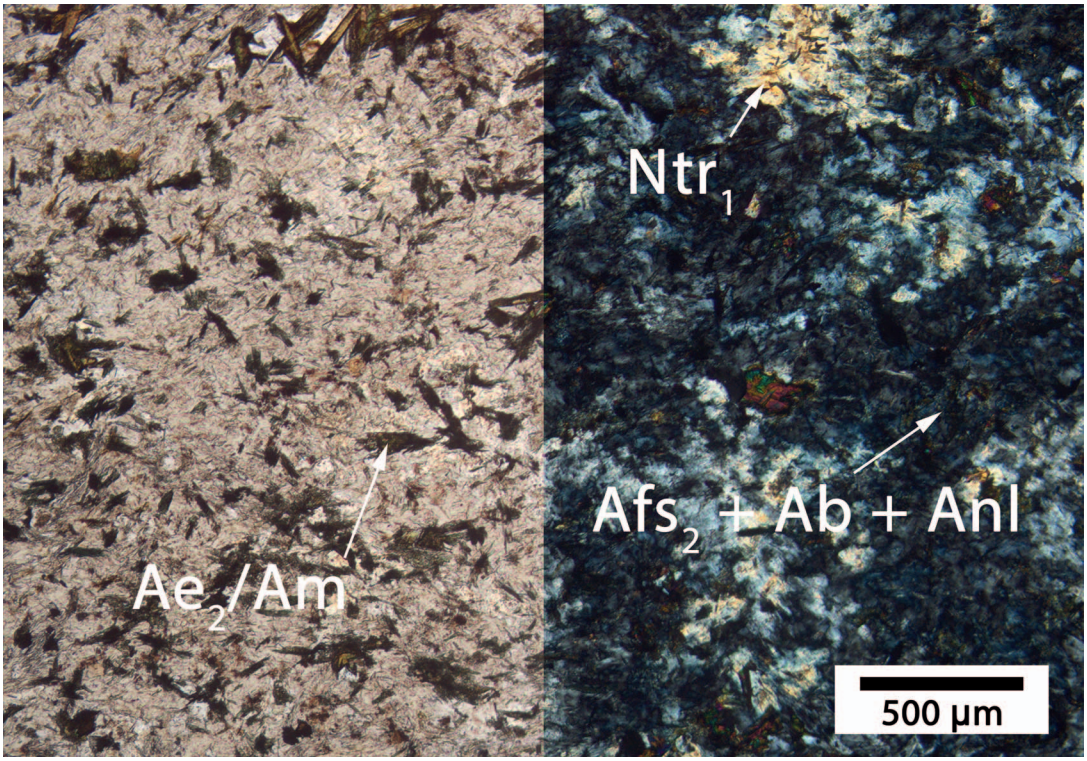

FIG. 10. Photomicrograph of the phonolite dike under plane-polarized light (PPL; left) and circularly polarized light (CPL). The dark felty regions in CPL are composed of alkali feldspar (Afs_2), albite (Ab), and analcime (Anl) intergrowths, whereas natrolite (Ntr_1) forms optically clear, clot-like patches. Aegirine (Ae_2) and sodic amphibole (Am) are evenly dispersed within the sample.

in contrast to those reported for aegirine from the agpaitic intrusion at Mont Saint-Hilaire (Québec). At Mont Saint-Hilaire, aegirine grains from various lithologies were found to have cores enriched in Ca + Zr and rims enriched in Na + Ti (Piilonen *et al.* 1998). Only two Mn-dominant minerals other than windmountainite were found in the polished thin section of the phonolite and these in trace abundances: schizolite, present at vesicle margins, and an unidentified Mn-oxy-hydroxide, which develops as black, anhedral to platy masses that appear to replace earlier-formed minerals.

Detailed examination of the vesicles shows that they contain an assemblage of albite, aegirine, neotocite, windmountainite, fluorapophyllite-(K), montmorillonite, and natrolite. The vesicles are commonly lined with white to colorless, euhedral crystals of albite and green, bladed crystals of aegirine, with windmountainite partially or completely spanning the void spaces. Locally, windmountainite is found to nucleate on neotocite, demonstrating that windmountainite is paragenetically later. Fluorapophyllite-(K) develops as colorless, striated, blocky crystals ranging in size from 0.3 × 0.3 mm to 3 × 3 mm; it both overgrows and contains inclusions of windmountainite, indicating it is paragenetically later. Locally, the tips of acicular sprays of windmountainite exhibit gradual bleaching from pale yellow to white. Powder X-ray diffraction analysis shows that these tips are composed of montmorillonite with traces of windmountainite. Montmorillonite additionally forms translucent to opaque, white to pale yellow crystals with a waxy luster; rarely, masses of sky-blue montmorillonite can be seen completely filling vesicles. When crystals of montmorillonite are noted, they are acicular to prismatic and arranged in bundles, resembling windmountainite. Given (1) the morphological similarities between windmountainite and montmorillonite; (2) the presence of a gradual, bleached contact relationship between the two; and (3) similarities in their crystal structures and chemistries, the montmorillonite is interpreted, at least in part, to be an alteration product of windmountainite (pseudomorph?), as opposed to being an overgrowth. Several

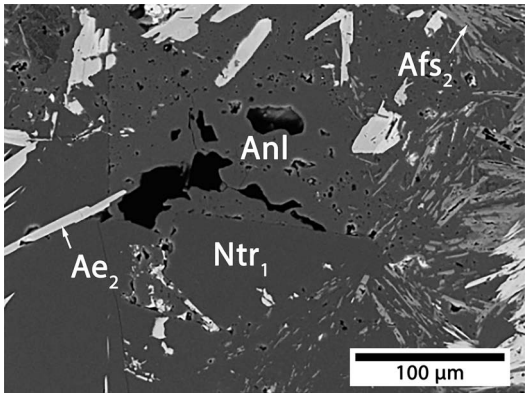

FIG. 11. Backscattered electron image of the phonolite dike, illustrating the sharp contact between natrolite (Ntr_1) and analcime (Anl), suggestive of an overgrowth relationship rather than one involving alteration. Euhedral alkali feldspar (Afs_2) and aegirine (Ae_2) indicate that both formed prior to or during the crystallization of Ntr_1 and Anl.

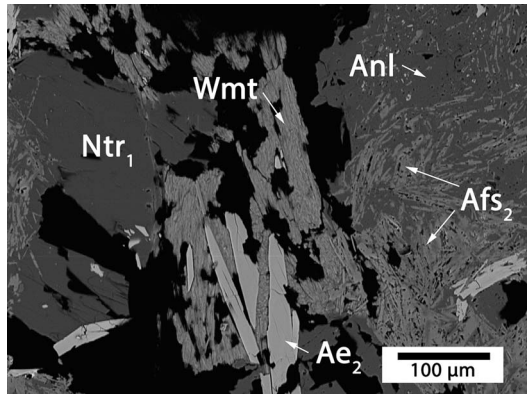

FIG. 12. Backscattered electron image of the phonolite dike proximal to vesicles. Alkali feldspar (Afs_2) and analcime (Anl) are commonly intergrown and pitted, whereas natrolite (Ntr_1) is rarely pitted. Note the sharp contact between windmountainite (Wmt) and aegirine (Ae_2). This, and the fact that windmountainite surrounds Ae_2, suggests that windmountainite is an overgrowth, and not an alteration product of Ae_2.

vesicles are partially or exclusively filled with either natrolite or an unidentified fine-grained orange to red phase, which appears to be the latest stage in the mineral paragenesis.

Given that aegirine is present in both the primary and secondary assemblages of the phonolite and represents the dominant Fe-bearing mineral in the secondary assemblage, the possibility that windmountainite represents an alteration of pre-existing aegirine must be considered. Examination of SEM-BSE images show that windmountainite overgrows aegirine; moreover, the contact between the two minerals is sharp (Fig. 12). This suggests that windmountainite is not a product related to the alteration of pre-existing aegirine.

Mineral chemistry of the phonolite dike

The mineral chemistry of major and minor rock-forming minerals occurring in the phonolite dike was determined by SEM-EDS using a JEOL 6400 SEM, an accelerating voltage of 20 kV, beam current of 1.0 nA, and counting times of 10 s. Data were processed using AZTEC software (Oxford Instruments, United Kingdom). Ten elements were analyzed for [analyte, (X-ray line, standard)]: Na ($K\alpha$, albite), Mg ($K\alpha$, diopside), Al ($K\alpha$, albite), Si ($K\alpha$, albite), K ($K\alpha$, wadeite), Ca ($K\alpha$, diopside), Ti ($K\alpha$, synthetic $CaTiO_3$), Mn ($K\alpha$, tephroite), and Fe ($K\alpha$, Fe metal), and Zr ($K\alpha$, Zr metal). Chemical formulae were calculated on the basis of ΣT (*i.e.*, Si + Al) for alkali feldspar ($\Sigma T = 4$ *apfu*), albite ($\Sigma T = 4$ *apfu*), natrolite ($\Sigma T = 5$ *apfu*), and analcime ($\Sigma T = 3$ *apfu*); $\Sigma(M + T$, *i.e.*, $Si + Al + Fe^{3+} + Mn^{2+} + Mg + Ca + \ldots) = 4$ *apfu* for aegirine; $Si = 3$ *apfu* for schizolite; and following the recommendations of Holland & Blundy (1994) for sodic amphibole. For aegirine and sodic amphibole, the valence of Fe was calculated based on charge balance.

Chemical data for the major and minor rock-forming minerals using SEM-EDS (Table 13) can be summarized in terms of the observed ranges in chemistry as follows:

alkali feldspar: $(K_{0.95–0.50}Na_{0.47–0.07})_{\Sigma 1.13–0.95}(Si_{3.00–2.96}Al_{1.04–1.00})_{\Sigma 4.00}O_8$,
albite: $(Na_{1.10–0.94}K_{0.08–0.03})_{\Sigma 1.18–0.97}(Si_{3.00–2.88}Al_{1.12–1.00})_{\Sigma 4.00}O_8$,
analcime: $(Na_{0.96–0.80}K_{0.09–0.00}Ca_{0.04–0.00})_{\Sigma 0.97–0.85}(Si_{2.04–2.01}Al_{0.99–0.96}Fe_{0.01–0.00})_{\Sigma 3.00}O_6 \cdot H_2O$,
natrolite: $(Na_{2.05–1.85}K_{0.02–0.00})_{\Sigma 2.05–1.85}(Si_{3.03–2.99}Al_{2.00–1.97}Fe_{0.01–0.00})_{\Sigma 5.00}O_{10} \cdot 2H_2O$,
aegirine (the dominant pyroxene species): $(Na_{1.01–0.82}Ca_{0.21–0.03})_{\Sigma 1.06–1.02}(Fe^{3+}_{0.83–0.60}Ti_{0.11–0.03}Al_{0.10–0.00}Fe^{2+}_{0.17–0.00}Mn_{0.07–0.01}Zr_{0.10–0.00}Mg_{0.04–0.00})_{\Sigma 0.98–0.94}(Si_{1.99–1.92}Al_{0.06–0.01}Fe^{3+}_{0.02–0.00})_{\Sigma 2.00}O_6$,
eckermannitic arfvedsonite to potassic-arfvedsonite (the dominant sodic amphibole species): $(Na_{0.85–0.34}K_{0.80–0.42})_{\Sigma 1.31–1.13}(Na_{2.00–1.75}Ca_{0.25–0.00})_{\Sigma 2.00}(Fe^{2+}_{3.77–3.24}Fe^{3+}_{0.57–0.13}Ti_{0.39–0.19}Mn_{0.48–0.13}Mg_{0.60–0.14}Al_{0.37–0.00}Zr_{0.15–0.00})_{\Sigma 4.97–4.69}(Si_{8.08–7.39}Al_{0.52–0.00})_{\Sigma 8.08–7.91}O_{22}(OH)_2$, and
schizolite: $(Na_{1.00–0.91}K_{0.09–0.00})_{\Sigma 1.00}(Ca_{0.83–0.73}Mn_{0.56–0.29}Fe_{0.27–0.15}Na_{0.23–0.12}Al_{0.22–0.00}Zr_{0.07–0.02})_{\Sigma 1.74–1.68}Si_{3.00}O_8(OH)$.

TABLE 13. MINERAL CHEMISTRY [AVERAGE (2σ)] OF MAJOR AND MINOR MINERALS IN PHONOLITE DIKE

wt.% oxide	Afs ($n = 9$)	Anl ($n = 12$)	Ntr ($n = 6$)	Ab ($n = 4$)	Am ($n = 7$)	Ae ($n = 12$)	Shz ($n = 4$)
K_2O	14.16 (4.68)	0.34* (1.02)	0.19* (-)	0.95 (0.85)	2.84 (1.66)	*bdl*	1.15* (0.33)
Na_2O	2.13* (3.06)	12.09 (2.17)	15.42 (1.42)	11.67 (1.54)	7.85 (0.72)	12.87 (1.78)	10.07 (0.62)
CaO	*bdl*	0.55* (0.56)	*bdl*	*bdl*	1.02* (0.74)	2.13 (2.78)	12.75 (2.29)
MgO	*bdl*	*bdl*	*bdl*	*bdl*	1.04 (1.34)	0.58* (0.27)	*bdl*
MnO	*bdl*	*bdl*	*bdl*	*bdl*	1.99 (1.96)	0.99 (0.97)	8.31 (4.91)
FeO^{tot}	*bdl*	0.28* (0.07)	0.25* (0.05)	*bdl*	28.11 (3.00)	25.12 (2.53)	4.35 (1.90)
TiO_2	*bdl*	*bdl*	*bdl*	*bdl*	2.37 (1.16)	2.03 (1.44)	*bdl*
ZrO_2	*bdl*	*bdl*	*bdl*	*bdl*	1.07* (0.82)	2.05* (3.51)	1.64 (1.62)
Al_2O_3	18.55 (0.64)	22.02 (1.75)	26.16 (0.69)	19.87 (2.03)	1.57 (1.51)	1.52 (1.12)	2.15* (2.06)
SiO_2	64.60 (1.21)	53.39 (3.25)	46.77 (0.90)	67.23 (2.90)	48.37 (4.42)	51.81 (1.98)	52.54 (3.00)
Total	99.44 (1.40)	88.20 (6.44)	88.47 (2.61)	99.72 (1.80)	95.48 (2.27)	97.52 (1.09)	92.14 (3.11)
apfu							
K	0.84	0.02	-	0.05	0.59	-	0.06
Na	0.19	0.88	1.92	1.00	2.47	0.95	1.12
Ca	-	0.01	-	-	0.15	0.09	0.78
Mg	-	-	-	-	0.25	0.01	-
Mn	-	-	-	-	0.28	0.03	0.39
Fe^{2+}	-	-	-	-	3.48	0.03	0.21
Fe^{3+}	-	-	-	-	0.34	0.77	-
Ti	-	-	-	-	0.29	0.06	-
Zr	-	-	-	-	0.05	0.02	0.05
Al	1.01	0.98	1.98	1.03	0.30	0.07	0.11
Si	2.99	2.02	3.01	2.97	7.85	1.98	3.00

* Analyses below detection limit (*bdl*) were not included in average or 2σ calculations for wt.% oxide data. Fe^{2+} and Fe^{3+} are calculated based on charge balance.
^{tot} Total FeO + Fe_2O_3 calculated as FeO.

Qualitative SEM analyses also indicate the presence of accessory minerals, including: fluorite, fluorapatite, a bastnaësite-group mineral, an unidentified Mn-oxy-hydroxide (manganite?), galena, and an unidentified Na-Zr-silicate with (Na+K+Ca):Zr:Si of 1.4:1:4 (catapleiite?). For comparison, the Aris phonolite from Namibia (Yakovenchuk *et al.* 2011) is similar in texture, mineralogy, *etc.*, to the phonolite at Wind Mountain (including the presence of palygorskite-group minerals in vesicles with bleached margins) and has endmember K-feldspar as the dominant feldspar, pyroxene that ranges from aegirine–augite to aegirine (as opposed to endmember aegirine at Wind Mountain), and natrolite approaching the endmember composition (similar to that at Wind Mountain).

Whole rock powder X-ray diffraction and Rietveld analysis of the phonolite dike

A fresh sample of the dike material was crushed in a tungsten carbide ring mill and whole-rock PXRD data were collected using a Scintag XDS 2000 automated diffractometer employing Cu$K\alpha_{avg}$ radiation ($\lambda = 1.5418$ Å), a 2θ range = 5–80°, a step size = 0.02°, and a dwell time/step = 8 s. The program Highscore Plus, ver. 3.3 (Panalytical BV, Netherlands) was used to identify the minerals present (using diffraction peaks) and to quantify their modal abundances *via* the Rietveld method.

Qualitatively, the PXRD pattern of the dike is a combination of major (albite, analcime, alkali feldspar, natrolite), minor (sodic amphibole, aegirine, and schizolite), and trace minerals (Mn-oxy-hydroxide, fluorite, and an apatite-group mineral). The .cif files of the minerals used in the Rietveld refinement are listed in Table 14. The sequence of fitting was based on the intensity of the strongest peaks to identify the major minerals present: albite, analcime, and alkali feldspar were refined first, including those parameters that could be refined (*e.g.*, lattice parameters, fractional coordinates, preferred orientation where applicable, *etc.*). Subsequent minerals were refined in the order natrolite, sodic amphibole (refined as potassic-arfvedsonite), aegirine, schizolite (refined as pectolite), Mn-oxy-hydroxide (refined as manganite), fluorite, and an apatite-supergroup mineral (refined as fluorapatite). Only one refinement was made and was refined to $R_{exp} = 3.68$, $R_p = 8.64$, $R_{wp} = 11.27$, and $GOOF = 9.37$.

TABLE 14. RIETVELD RESULTS OF WHOLE-ROCK POWDER X-RAY DIFFRACTION DATA OF PHONOLITE AT WIND MOUNTAIN

Mineral	R_{Bragg}	Modal %	*.CIF file reference
Microcline (Afs)	4.07	34	Blasi *et al.* (1987)
Anl	5.01	21	Ferraris *et al.* (1972)
Ntr	4.56	21	Capitelli & Derebe (2007)
Ab	4.29	17	Prewitt *et al.* (1976)
Potassic-arfvedsonite (Am)	4.19	2	Pekov *et al.* (2004)
Ae	6.91	2	Redhammer *et al.* (2006)
Pectolite (Shz)	4.65	2	Takeuchi & Kodoh (2015)
Manganite (Mn-oxy-hydroxide)	3.72	<1	Buerger (1936)
Fluorite	3.75	<1	Cheetham *et al.* (1971)
Fluorapatite	9.86	<1	Andreev (1994)
Total		100	

Abbreviations: Ab = albite, Ae = aegirine, Afs = alkali feldspar, Am = sodic amphibole, Anl = analcime, Ntr = natrolite, Shz = schizolite.

Normalized QAPF mineralogy, calculated using the modal data derived from Rietveld analysis, shows the phonolite should be classified as a natrolite analcime syenite (Streckeisen 1974). Results are similar to, but distinct from, those of other alkaline igneous environments where palygorskite-group minerals have been found: (1) the Aris phonolite (Namibia) additionally contains nepheline and sodalite but lacks analcime, albite, and sodic amphibole (Yakovenchuk *et al*. 2011); whereas (2) the Saint Amable sill (Québec) additionally contains nepheline but contains considerably less analcime and sodic amphibole (Horváth *et al*. 1998). The phonolites from all three localities are classified as feldspathoid syenites; however, nepheline is virtually absent in the phonolite at Wind Mountain (only rare phenocrysts of nepheline were reported in the dike; McLemore *et al*. 1996), which makes it unique among those phonolites being considered. The prevalence of hydrated feldspathoids (natrolite and analcime), as opposed to nepheline, in the Wind Mountain phonolite dike is suggestive of higher $a\mathrm{H_2O}$, $a\mathrm{SiO_2}$, and lower $a\mathrm{Al_2O_3}$ in the melt from which the phonolite developed at Wind Mountain.

Semi-quantitative whole-rock geochemical data were calculated using the modal mineralogy derived from Rietveld analysis and the mineral chemistry. The geochemical data indicate that the phonolite dike can be classified as phonolite, or its intrusive equivalent, a foid syenite, based on the total alkali-silica classification (Le Maitre *et al*. 2002, Middlemost 1994), a feature consistent with the petrological classification based on the modal mineralogy obtained by Rietveld refinement of the PXRD data. Furthermore, the calculated agpaitic index [mol.% (Na+K)/Al] was found to be 1.03, which is within the corresponding values for Wind Mountain (0.92–1.08; calculated using data from McLemore *et al*. 1996). The agpaitic index for the phonolite dike marginally exceeds 1 (*i.e*., it can be considered as being weakly peralkaline). This, combined with the rarity of HFSE-bearing minerals (*e.g*., eudialyte-group minerals, catapleiite, *etc*.), suggests the phonolite dike may be considered marginally miaskitic.

Paragenesis of the phonolite dike and the origin of windmountainite

The paragenetic sequence of the phonolite dike at Wind Mountain (Fig. 13) can be divided into two stages: (1) a primary sequence of rock-forming minerals and (2) a secondary sequence, reflecting minerals that develop in vesicles, likely from trapped, late-stage fluids. Windmountainite clearly develops in the secondary stage; however, it is necessary to consider the complete paragenetic sequence of the host phonolite dike, so as to effectively interpret the origin of windmountainite and the conditions facilitating its formation.

The primary sequence begins with the crystallization of alkali feldspar$_1$ (subscripts denote different generations of the same mineral), aegirine$_1$, annite, and the unidentified dark-red mineral, based on their occurrence as phenocrysts to the matrix minerals (*e.g*., aegirine$_2$, alkali feldspar$_2$, albite, sodic amphibole, natrolite$_1$, and analcime). Natrolite$_1$ is typically subhedral and appears to crystallize later than most of the earliest matrix minerals, but earlier than some aegirine grains (which are interstitial to natrolite$_1$). The occurrence of aegirine$_2$ in two habits (interstitial anhedral and prismatic to bladed), along with the observed chemical zoning evident in prismatic aegir-

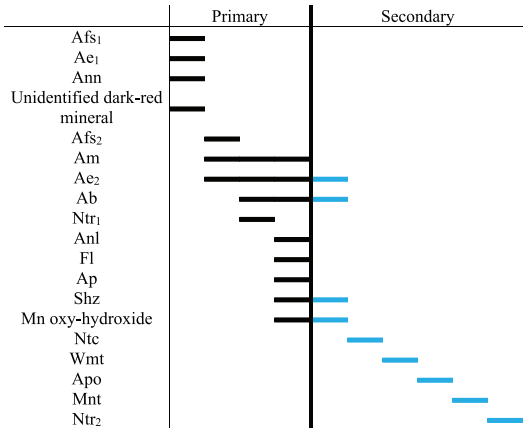

FIG. 13. Mineral paragenetic sequence of the Wind Mountain phonolite dike. Subscripts represent different generations where minerals appear more than once in the sequence. Abbreviations: Ab = albite, Afs = alkali feldspar, Ae = aegirine, Am = sodic amphibole, Anl = analcime, Ann = annite, Ap = fluorapatite, Apo = fluorapophyllite-(K), Fl = fluorite, Mnt = montmorillonite, Ntc = neotocite, Ntr = natrolite, Shz = schizolite, and Wmt = windmountainite.

ine (*i.e.*, elevated Zr content in rims) suggest that aegirine grew over an extended period of crystal fractionation. Despite the similarity in habits between sodic amphibole and aegirine$_2$, there is no compelling textural evidence of replacement of sodic amphibole by aegirine$_2$ or *vice-versa*, so sodic amphibole is considered to have formed contemporaneously with aegirine$_2$, as a function of the local geochemistry. Analcime is pitted and generally interstitial anhedral to subhedral, suggesting that it may be a later alteration product. The alkali feldspar$_2$ is also pitted, but it develops in subhedral to euhedral crystals. The pitting observed in both analcime and alkali feldspar$_2$ may suggest they are products of a volume-reducing reaction (alteration or coupled dissolution–precipitation, CPD; Putnis 2002). Schizolite is found at the margins of the vesicles and is interpreted to represent the transition between primary and secondary assemblages. Manganese-oxy-hydroxides appear to replace earlier phases and are therefore considered to be paragenetically late in the primary assemblage.

The secondary sequence consists of late primary minerals (aegirine$_2$, albite, schizolite) followed by neotocite, windmountainite, fluorapophyllite-(K), montmorillonite, and natrolite$_2$. The dominant Fe-bearing minerals in the secondary assemblage are aegirine$_2$ and windmountainite (Fig. 13). As noted earlier, the aegirine$_2$ appears primary and fresh (*i.e.*, little to no evidence of alteration) and the evidence clearly shows that windmountainite is not an alteration product arising through the breakdown of aegirine$_2$. Windmountainite occurs paragenetically earlier than fluorapophyllite-(K), given its occurrence as inclusions in the latter. The presence of fluorapophyllite-(K), a Ca-, K-, and F-rich mineral, suggests that the activities of Ca, K, and F increased after the crystallization of windmountainite, possibly due to the introduction of a later-stage, Ca-, K-, and F-rich fluid. Fluorine-bearing species are present before and after windmountainite in the paragenetic sequence [fluorite, fluorapatite, and fluorapophyllite-(K)]; however, F was found to be absent in windmountainite, despite compositions containing minor Cl. Windmountainite contains substantial Fe^{3+} (20.17 wt.% Fe_2O_3) and, given that palygorskite-group minerals share structural similarities with mica-group minerals (*i.e.*, homologous *T-O-T* modules), the Fe-F avoidance rule that has been invoked to exert a crystal-chemical control on the chemistry of crystallizing ferromagnesian minerals (*e.g.*, mica-group minerals; Mason 1992) could partially explain the absence of F in windmountainite. Montmorillonite post-dates windmountainite and fluorapophyllite-(K); crystal-chemical similarities between montmorillonite and windmountainite, along with the absence of a sharp contact between the two, suggests that montmorillonite replaces windmountainite. The transformation between palygorskite and smectite has been documented in sedimentary environments and has been shown experimentally to be a coupled-dissolution–epitaxial-precipitation reaction (Krekeler *et al.* 2005), which is compatible with the observations made in this study. In sedimentary environments, smectite minerals (such as montmorillonite) are more stable under conditions of higher pH (>9.5) and higher alkali salinity than palygorskite (Jones & Galán 1988, Guggenheim & Krekeler 2011). This suggests that after windmountainite crystallized, an increase in alkalinity may have led to its destabilization and the formation of montmorillonite. The late-stage development of a second generation of natrolite (*i.e.*, natrolite$_2$) in vesicles represents the last mineral in the paragenesis; this is also observed at Saint-Amable (Horváth *et al.* 1998) and Aris (von Knorring & Franke 1987). The formation of late natrolite in vesicles could be the result of later-stage hydrothermal activity, as is suggested by Horváth *et al.* (1998).

The vesicles in the phonolite are noted to have distinct, bleached margins that could be produced by (1) the production of secondary clays *via* alteration, (2) pitting or grain-size reduction *via* alteration, or (3) changes in the hydration state of the minerals present (*e.g.*, natrolite). Bleaching caused by the development of secondary clays is ruled out, as no clays were detected by optical petrography, qualitative SEM-

EDS, or PXRD methods. Similarly, bleaching produced by pitting or grain-size reduction is unlikely to be responsible, as no significant changes in mineralogy in relation to the distance of the bleaching from the vesicle were noted. Given that natrolite is an important mineral in the host phonolite, changes involving natrolite could influence the rock appearance. There are at least three known natrolite-like minerals, including natrolite, paranatrolite, and gonnardite, which differ in symmetry and H_2O content. At Mont Saint-Hilaire (Québec), it has been observed that upon exposure to air, transparent, lustrous, colorless crystals of paranatrolite readily and irreversibly transform to dull white, opaque crystals of gonnardite (Chen & Chao 1980, Chao 1980). This conversion involves dehydration, and the white, opaque appearance of gonnardite is reminiscent of the bleaching zones around the vesicles of the phonolite at Wind Mountain. The analytical methods used to verify the natrolite (whole-rock PXRD, SEM-EDS) in this study are of insufficient resolution to reliably distinguish between natrolite, paranatrolite, and gonnardite. Therefore, the exact mineral species (single or multiple) present in the phonolite, both outside and within the bleached zones, cannot be determined unequivocally. It is therefore plausible that the bleaching around the vesicles in the phonolite at Wind Mountain may be attributable to dehydration reactions involving natrolite or one of the natrolite-related minerals. However, more data are required to substantiate this claim.

Given that H_2O is critical to the stabilization of palygorskite-group minerals, the origin of hydrated feldspathoids in the phonolite dike at Wind Mountain is relevant to the genesis of windmountainite. At Aris, the formation or development of natrolite and analcime have been variably interpreted as alteration products of nepheline and sodalite (Koller *et al*. 2013, Yakovenchuk *et al*. 2011), and at Saint-Amable, primary natrolite has been reported, whereas analcime is interpreted to be an alteration product of nepheline (Horváth *et al*. 1998). Our textural interpretations of natrolite and analcime in the phonolite dike at Wind Mountain are consistent with those suggested for the Saint-Amable sill; *i.e*., natrolite is a primary rock-forming mineral and analcime is an alteration product of precursor feldspathoids. This may further imply that the phonolites at both localities arose from similar formational processes.

Palygorskite-group minerals are generally considered to develop under oxidizing, H_2O-bearing, alkaline conditions. All Fe-bearing palygorskite-group minerals, including tuperssuatsiaite, yofortierite, and windhoekite, have been found to be dominated by Fe^{3+}, based on data from mineral chemistry, SCXRD, and Mössbauer spectroscopy (Cámara *et al*. 2002, Huang *et al*. 2007, Hawthorne *et al*. 2013, Chukanov *et al*. 2012). This implies that these minerals generally develop under conditions of relatively high fO_2, although the specific conditions or range in conditions are not known. Structurally bound H_2O clearly stabilizes the structure of palygorskite (Post & Heaney 2008), so a high aH_2O must also be considered requisite to the formation of palygorskite-group minerals in general. Moreover, these minerals are found in vesiculated cavities (some of which can be fluid-filled, such as those from the Aris Quarry; Kolitsch *et al*. 2016) and are commonly associated with hydrated minerals, which suggests that H_2O-bearing fluids were present during their formation. In carbonate soils, palygorskite is known to form under conditions of high pH, specifically 9 to 11 (Verrecchia & Coustumer 1996); this suggests that strongly basic conditions likely favor the stability of palygorskite-group minerals in general. In summary, the occurrence of windmountainite and the crystal-chemistry of palygorskite-group minerals indicate that windmountainite likely developed as a product of basic, oxidized, Fe^{3+}- and H_2O-bearing alkaline fluids.

Conclusions

1. Windmountainite is a new member of the palygorskite group from Wind Mountain, Otero County, New Mexico, USA, having the simplified formula $\square Fe^{3+}{}_2Mg_2\square_2Si_8O_{20}(OH)_2(H_2O)_4{\cdot}4H_2O$. It has a modulated, layered-like crystal structure, which is a hybrid between that of a double-chain inosilicate (*e.g*., amphibole) and phyllosilicate (*e.g*., mica). Its crystal structure is based on *T-O-T* modules developed from inverted double chains of SiO_4 tetrahedra that sandwich ribbons of $M\varphi_6$ octahedra (φ = O, OH, H_2O, Cl), leading to large channels ($\sim$6.5 × 9 Å) that are occupied by loosely held H_2O groups.
2. The proposed classification scheme for the palygorskite group [general structural formula $M1M2_2M3_2M4_2T1_4T2_4O_{20}(OH)_2(H_2O,OH)_4{\cdot}W$] is developed based on the cations that occupy the *M*1-*M*2-*M*3-*M*4 sites. In this context, palygorskite is the □-Al-Mg-□ endmember and windmountainite the □-Fe^{3+}-Mg-□ endmember. It is argued that raite should be included in the palygorskite group due to its structural and crystal-chemical similarities.
3. The host phonolite dike can be classified as a natrolite analcime syenite, and the dominance of hydrated feldspathoids is suggestive of relatively higher aH_2O, $aSiO_2$, and lower aAl_2O_3 in the melt from which the phonolite crystallized, when compared to those from phonolites associated with other alkaline igneous complexes (*e.g*., Aris

phonolite and Saint Amable sill) where palygorskite-group minerals have been found.

4. Windmountainite occurs in vesicles with bleached haloes and is associated with albite, aegirine, fluorapophyllite-(K), natrolite, neotocite, and montmorillonite. It likely formed in the presence of late-stage, basic, oxidized, Fe^{3+}- and H_2O-bearing, alkaline hydrothermal fluids.

Acknowledgments

We would like to thank Mr. Bobby Jones for providing access to the site, Dr. Kirk C. Ross for assistance with collecting EMPA data, Mr. Mark A. Cooper (University of Manitoba) for collecting SCXRD data, Prof. Frank C. Hawthorne (University of Manitoba) for providing access to the three-circle diffractometer lab at the University of Manitoba, and Prof. Joy Gray-Munro (Laurentian University) for collecting FTIR data. Two anonymous reviewers are thanked for their comments.

References

Akbulut, A. & Kadir, S. (2003) The geology and origin of sepiolite, palygorskite, and saponite in Neogene lacustrine sediments of the Serinhisar-Acipayam basin, Denizli, SW Turkey. *Clays and Clay Minerals* **51(3)**, 279–292.

Andreev, Y.G. (1994) The use of the serial-correlations concept in the figure-of-merit function for powder diffraction profile fitting. *Journal of Applied Crystallography* **27(3)**, 288–297.

Anthony, J.A., Bideaux, R.A., Bladh, K.W., & Nichols, M.C., Eds. (2001) *Handbook of Mineralogy*. Mineralogical Society of America, Chantilly, Virginia, United States.

Artioli, G. & Galli, E. (1994) The crystal structures of orthorhombic and monoclinic palygorskite. *Materials Science Forum* **166–169**, 647–652.

Augsburger, M.S., Strasser, E., Perino, E., Mercader, R.C., & Pedregosa, J.C. (1998) FTIR and Mossbauer investigation of a substituted palygorskite: Silicate with a channel structure. *Journal of Physics and Chemistry of Solids* **59(2)**, 17–180.

Bailey, S.W. (1980) Summary of recommendations of AIPEA nomenclature committee on clay minerals. *American Mineralogist* **65**, 1–7.

Bailey, S.W., Frank-Kamenetskii, V.A., Goldsztaub, S., Kato, A., Pabst, A., Shulz, H., Taylor, H.F.W., Fleischer, M., & Wilson, A.J.C. (1977) International Union of Crystallography: Report of the International Mineralogical Association (IMA) –International Union of Crystallography (IUCr) Joint Committee on Nomenclature. *Acta Crystallographica* **A33**, 681–684.

Barker, D.S. & Hodges, F.N. (1977) Mineralogy of intrusions in the Diablo Plateau, northern Trans-Pecos magmatic province, Texas and New Mexico. *Geological Society of America Bulletin* **88**, 1428–1436.

Baur, W.H. (1974) The geometry of polyhedral distortions: Predictive relationships for the phosphate group. *Acta Crystallographica B* **30**, 1195–1215.

Blasi, A., De Pol Blasi, C., & Zanazzi, P.F. (1987) A re-examination of the Pellotsalo microcline: Mineralogical implications and genetic considerations. *Canadian Mineralogist* **25**, 527–537.

Boggs, R.C. (1985) Mineralogy of the Wind Mountain laccolith, Otero County, New Mexico. *New Mexico Geology* **6**, 41–42 (abstract).

Boggs, R.C. & Ghose, S. (1985) Georgechaoite NaKZr $Si_3O_9 \cdot 2H_2O$, a new mineral species from Wind Mountain, New Mexico. *Canadian Mineralogist* **23**, 1–4.

Bradley, W.F. (1940) The structural scheme of attapulgite. *American Mineralogist* **25(6)**, 405–410.

Brese, N.E. & O'Keeffe, M. (1991) Bond-valence parameters for solids. *Acta Crystallographica* **B47**, 192–197.

Buerger, M.J. (1936) The symmetry and crystal structure of manganite, Mn(OH)O. *Zeitschrift für Kristallographie* **95**, 163–174.

Callen, R.A. (1984) Clays of the palygorskite-sepiolite group: Depositional environment, age and distribution. *Developments in Sedimentology* **37**, 1–37.

Cámara, F., Garvie, L.A.J., Devouard, B., Groy, T.L., & Buseck, P.R. (2002) The structure of Mn-rich tuperssuatsiaite: A palygorskite-related mineral. *American Mineralogist* **87(10)**, 1458–1463.

Capitelli, F. & Derebe, M.G. (2007) Single crystal X-ray diffraction study of a pure natrolite sample. *Journal of Chemistry and Crystallography* **37**, 583–586.

Chao, G.Y. (1980) Paranatrolite, a new zeolite from Mont St-Hilaire, Québec. *Canadian Mineralogist* **18**, 86–88.

Cheetham, A.K., Fender, B.E.F., & Cooper, M.J. (1971) Defect structure of calcium fluoride containing excess anions: I. Bragg scattering. *Journal of Physics C: Solid State Physics* **4**, 3107–3121.

Chen, T.T. & Chao, G.Y. (1980) Tetranatrolite from Mont St-Hilaire, Québec. *Canadian Mineralogist* **18**, 77–84.

Chiari, G., Giustetto, R., & Ricchiardi, G. (2003) Crystal structure refinements of palygorskite and Maya Blue from molecular modelling and powder synchrotron diffraction. *European Journal of Mineralogy* **15**, 21–33.

Christ, C.L., Hathaway, J.C., Hostetler, P.B., & Shepard A.O. (1969) Palygorskite: New X-ray data. *American Mineralogist* **354(1)**, 198–205.

Chryssikos, G.D., Gionis, V., Kacandes, G.H., Stathopoulou, E.T., Suárez, M., García-Romero, E., & Del Rio, M.S. (2009) Octahedral cation distribution in palygorskite. *American Mineralogist* **94(1)**, 200–203.

Chukanov, N.V., Britvin, S.N., Blass, G., Belakovskiy, D.I., & Van, K.V. (2012) Windhoekite, $Ca_2Fe^{3+}_{3-x}(Si_8O_{20})(OH)_4{\cdot}10H_2O$, a new palygorskite-group mineral from the Aris phonolite, Namibia. *European Journal of Mineralogy* **24(1)**, 171–179.

Clabaugh, S.E. (1941) *Geology of the Northwestern Portion of the Cornudas Mountains, New Mexico*. M.Sc. Thesis, University of Texas, Austin, Texas, United States.

Coombs, D.S., Alberti, A., Armbruster, T., Artioli, G., Colella, C., Galli, E., Grice, J.D., Liebau, F., Mandarino, J.A., Minato, H., Nickel, E.H., Passaglia, E., Peacor, D.R., Quartieri, S., Rinaldi, R., Ross, M., Sheppard, R.A., TillManns, E., & Vezzalini, G. (1997) Recommended nomenclature for zeolite minerals: Report of the subcommittee on zeolites of the International Mineralogical Association, Commission on New Minerals and Mineral Names. *Canadian Mineralogist* **35**, 1571–1606.

Ferraris, G. & Gula, A. (2005) Polysomatic aspects of microporous minerals – Heterophyllosilicates, palysepioles and rhodesite-related structures. *Reviews in Mineralogy & Geochemistry* **57**, 69–104.

Ferraris, G., Jones, D.W., & Yerkess, J. (1972) A neutron-diffraction study of the crystal structure of analcime, $NaAlSi_2O_6{\cdot}H_2O$. *Zeitschrift für Kristallographie* **135**, 240–252.

Fischer, R.X., Burianek, M., & Shannon, R.D. (2018) *POLARIO*, a computer program for calculating refractive indices from chemical compositions. *American Mineralogist* **103(8)**, 1345–1348.

Gaines, R.V., Skinner, H.C.W., Foord, E.E., Mason, B., & Rosenzweig, A. (1997) *Dana's New Mineralogy: The System of Mineralogy of James Dwight Dana and Edward Salisbury Dana*. 8th Edition, John Wiley & Sons, Toronto, Ontario, Canada.

Grice, J.D., Lussier, A.J., Friis, H., Rowe, R., Poirier, G.G., & Fihl, Z. (2019) Discreditation of the pyroxenoid mineral name 'marshallsussmanite' with a reinstatement of the name schizolite, $NaCaMnSi_3O_8(OH)$. *Mineralogical Magazine* **83**, 473–478.

Guggenheim, S. & Krekeler, M.P.S. (2011) The structures and microtextures of the palygorskite-sepiolite group minerals. *In* Developments in Clay Science: Developments in Palygorskite-Sepiolite Research **3** (E. Galan, A. Singer, eds.). Elsevier, Amsterdam, Netherlands (3–32).

Hawthorne, F.C., Oberti, R., Harlow, G.E., Maresch, W.V., Martin, R.F., Schumacher, J.C., & Welch, M.D. (2012) Nomenclature of the amphibole supergroup. *American Mineralogist* **97**, 2031–2048.

Hawthorne, F.C., Abdu, Y.A., Tait, K.T., & Back, M.E. (2013) The crystal structure of yofortierite. *Canadian Mineralogist* **51(2)**, 243–251.

Hendricks, S.B. & Jefferson, M.E. (1939) Polymorphism of the micas. *American Mineralogist* **24(12)**, 729–772.

Holland, T. & Blundy, J. (1994) Non-ideal interactions in calcic amphiboles and their bearing on amphibole-plagioclase thermometry. *Contributions to Mineralogy and Petrology* **116**, 433–447.

Horváth, L., Pfenninger-Horváth, E., Gault, R.A., & Tarasoff, P. (1998) Mineralogy of the Saint-Amable sill. *Mineralogical Record* **29(2)**, 83–118.

Huang, Y., Li, Z., Li, S., Shi, Z., Lin, Y., & Hsia, Y. (2007) Mössbauer investigations of palygorskite from Xuyi, China. *Nuclear Instruments and Methods in Physics Research Section B: Interactions with Materials and Atoms* **260(2)**, 657–662.

Jones, B.F. & Galán, E. (1988) Sepiolite and palygorskite. *In* Hydrous Phyllosilicates (Exclusive of the Micas) (S.W. Bailey, ed.). *Reviews in Mineralogy* **19**, Mineralogical Society of America, Washington, D.C., United States (631–674).

Karup-Møller, S. & Petersen, O.V. (1984) Tuperssuatsiaite, a new mineral species from the Ilimaussaq intrusion in south Greenland. *Neues Jahrbuch für Mineralogie Monatshefte* **1984**, 501–512.

Kolitsch, U., Blaß, G., Jahn, S., Cámara, F., von Bezing, L., Wartha, R.R., Tremmel, G., Sturla, M., Cerea, P., Skebo, M., & Ciriotti, M.E. (2016) *Aris: Mineralogy of the famous alkaline phonolite*. Associazione Micromineralogica Italiana, Gioconda, Italy.

Koller, F., Škoda, R., Palfi, G., & Popp, F. (2013) Phonolites of the Aris and Rehoboth areas, Central Namibia. Mineralogická a petrologická konferencia MinPet 2013, 23–24 May 2013, Bratislava, Czech Republic, Zborník recenzovaných abstraktov príspevkov, 40.

Kraus, W. & Nolze, G. (1996) *Powder Cell* – a program for the representation and manipulation of crystal structures and calculation of the resulting X-ray powder patterns. *Journal of Applied Crystallography* **29**, 301–303.

Krekeler, M.P.S., Hammerly, E., Rakovan, J., & Guggenheim, S. (2005) Microscopy studies of the palygorskite-to-smectite transformation. *Clays and Clay Minerals* **53(1)**, 92–99.

Le Maitre, R.W., Streckeisen, A., Zanettin, B., Le Bas, M.J., Bonin, B., Bateman, P., Bellieni, G., Dudek, A., Efremova, S., Keller, J., Lameyre, J., Sabine, P.A., Schmid, R., Sørensen, H., & Woolley, A.R. (2002) *Igneous Rocks: A Classification and Glossary of Terms: Recommendations of the International Union of Geological Sciences Subcommission on the Systematics of Igneous Rocks*. Cambridge University Press, Cambridge, England.

MARKS, M.A.W. & MARKL, G. (2017) A global review on agpaitic rocks. *Earth Science Reviews* **173**, 229–258.

MASON, R.A. (1992) Models of order and iron-fluorine avoidance in biotite. *Canadian Mineralogist* **30**, 343–354.

MCARDLE, P., GILLIGAN, K., CUNNINGHAM, D., DARK, R., & MAHON, M. (2004) OSCAIL. *Crystal Engineering Communications* **6**, 303–309.

MCLEMORE, V.T. (2018) Rare earth elements (REE) deposits associated with Great Plain Margin deposits (alkaline-related), southwestern United States and eastern Mexico. *Resources* **7(1)**, 8.

MCLEMORE, V.T. & GUILINGER, J.R. (1993) Geology of mineral resources of the Cornudas Mountains, Otero County, New Mexico and Hudspeth County, Texas. *In* Carlsbad Region, New Mexico and Texas (D.L. Love, J.W. Hawley, B.S. Kues, J.W. Adams, G.S. Austin, & J.M. Barker, eds.). *New Mexico Geological Society Guidebook* **44**, 145–153.

MCLEMORE, V.T., LUETH, V.W., PEASE, T.C., & GUILINGER, J.R. (1996) Petrology and mineral resources of the Wind Mountain laccolith, Cornudas Mountains, New Mexico and Texas. *Canadian Mineralogist* **34**, 335–347.

MER'KOV, A.N., BUSSEN, I.V., GOYKO, Y.A., KUL'CHITSKAYA, Y.A., MEN'SHIKOV, Y.P., & NEDOREZOVA, A.P. (1973) Raite and zorite, new minerals from the Lovozero Tundra. *International Geology Review* **15**, 1087–1094.

MIDDLEMOST, E.A.K. (1994) Naming materials in the magma/igneous rock system. *Earth Science Reviews* **37(3–4)**, 215–224.

MOMMA, K. & IZUMI, F. (2008) *VESTA*: a three-dimensional visualization system for electronic and structural analysis. *Journal of Applied Crystallography* **41(3)**, 653–658.

NESPOLO, M. & BOUZNARI, K. (2017) Modularity of crystal structures: a unifying model for the biopyribole-palysepiole series. *European Journal of Mineralogy* **29(3)**, 369–383.

PEKOV, I.V., CHUKANOV, N.V., LEBEDEVA, Y.S., PUSHCHAROVSKII, D.Y., FERRARIS, G., GULA, A., ZADOV, A.E., NOVAKOVA, A.A., & PETERSEN, O.V. (2004) Potassicarfvedsonite, $KNa_2Fe^{2+}{}_4Fe^{3+}Si_8O_{22}(OH)_2$, a K-dominant amphibole of the afvedsonite series from agpaitic pegmatites – Mineral data, structure refinement and disorder in the A site. *Neues Jahrbuch für Mineralogie Monatshefte* **12**, 555–574.

PERRAULT, G., HARVEY, Y., & PERTSOWSKI, R. (1975) La yofortierite, un nouveau silicate hydrate de manganese de St-Hilaire, P.Q. *Canadian Mineralogist* **13(1)**, 68–74.

PETRUS, J.A., ROSS, K.C., & MCDONALD, A.M. (2012) *DIIS*: A cross-platform program for the reduction of X-ray diffraction data from a cylindrical area detector. *Computers & Geosciences* **38**, 156–163.

PIILONEN, P.C., MCDONALD, A.M., & LALONDE, A.E. (1998) The crystal chemistry of aegirine from Mont Saint-Hilaire, Québec. *Canadian Mineralogist* **36**, 779–791.

PLUTH, J.J., SMITH, J.V., PUSHCHAROVSKII, D.Y., SEMENOV, E.I., BRAM, A., RIEKEL, C., WEBER, H.-P., & BROACH, R.W. (1997) Third-generation synchrotron X-ray diffraction of 6-μm crystal of raite, $\approx Na_3Mn_3Ti_{0.25}Si_8O_{20}(OH)_2{\cdot}10H_2O$, opens up new chemistry and physics of low-temperature minerals. *Proceedings of the National Academy of Sciences of the United States of America* **94**, 12263–12267.

POST, J.E. & HEANEY, P.J. (2008) Synchrotron powder X-ray diffraction study of the structure and dehydration behaviour of palygorskite. *American Mineralogist* **93**, 667–675.

POVONDRA, P. (1996) Minerals of the hisingerite-neotocite series from Chvaletice, Železné hory Mts., eastern Bohemia, Czech Republic. *Journal of the Czech Geological Society* **41(1–2)**, 7–14.

PREWITT, C.T., SUENO, S., & PAPIKE, J.J. (1976) The crystal structures of high albite and monalbite at high temperatures. *American Mineralogist* **61**, 1213–1225.

PUSHCHAROVSKII, D.Y., PEKOV, I.V., PLUTH, J., SMITH, J., FERRARIS, G., VINOGRADOVA, S.A., ARAKCHEEVA, A.V., SOBOLEVA, S.V., & SEMENOV, E.I. (1999) Raite, manganonorderite-(Ce), and ferronordite-(Ce) from the Lovozero Massif: Crystal structures and mineralogical geochemistry. *Crystallographic Reports* **44(4)**, 565–574.

PUTNIS, A. (2002) Mineral replacement reactions: From macroscopic observations to microscopic mechanisms. *Mineralogical Magazine* **66(5)**, 689–708.

REDHAMMER, G.J., AMTHAUER, G., ROTH, G., TIPPELT, G., & LOTTERMOSER, W. (2006) Single-crystal X-ray diffraction and temperature dependent ^{57}Fe Mossbauer spectroscopy on the hedenbergite-aegirine $(Ca,Na)(Fe^{2+},Fe^{3+})Si_2O_6$ solid solution. *American Mineralogist* **91**, 1271–1292.

RUIZ-GALENDE, P., TORRE-FDEZ, I., ARAMENDIA, J., GOMEZ-NUBLA, L., CASTRO, K., ARANA, G., FDEZ-ORTIZ DE VALLEJUELO, S., MAGUREGUI, M., MEDINA, J., BAONZA, V.G., RULL, F., & MADARIAGA, J.M. (2019) New Raman-visible near-infrared database of inorganic and mineralogical planetary and terrestrial compounds and its implications for Mars: Phyllosilicates. *Journal of Raman Spectroscopy* **2019**, 1–11.

SCHÖNENBERGER, J. & MARKL, G. (2008) The magmatic and fluid evolution of the Motzfeldt Intrusion in South Greenland: Insights into the formation of agpaitic and miaskitic rocks. *Journal of Petrology* **49(9)**, 1549–1577.

SHANNON, R.D. (1976) Revised effective ionic radii and systematic studies of interatomic distances in halides and chalcogenides. *Acta Crystallographica* **A32(5)**, 751–767.

SHELDRICK, G.M. (1997) *SHELXL-97*: A computer program for the refinement of crystal structures. University of Göttingen, Göttingen, Germany.

SHELDRICK, G.M. (2008) *SADABS*. University of Göttingen, Göttingen, Germany.

SHELDRICK, G.M. (2015) Crystal structure refinement with *SHELXL*. *Acta Crystallographica* **C71(1)**, 3–8.

SMITH, J.V. & BAILEY, S.W. (1963) Second review of Al–O and Si–O tetrahedral distances. *Acta Crystallographica* **16**, 801–811.

STRECKEISEN, A. (1974) Classification and Nomenclature of Plutonic Rocks: Recommendations of the IUGS Subcommission on the Systematics of Igneous Rocks. *Geologische Rundschau* **63**, 773–786.

STRUNZ, H. & NICKEL, E. (2001) *Strunz Mineralogical Tables*. 9th Edition, Schweizerbart Science Publishers, Stuttgart, Germany.

SUÁREZ, M. & GARCÍA-ROMERO, E. (2011) Advances in the crystal chemistry of sepiolite and palygorskite. *In* Developments in Clay Science: Developments in Palygorskite-Sepiolite Research **3** (E. Galan & A. Singer, eds.). Elsevier, Amsterdam, Netherlands (33–65).

TAKEUCHI, Y. & KODOH, Y. (2015) Hydrogen bonding and cation ordering in Magnet Cove pectolite. *Zeitschrift für Kristallographie – Crystalline Materials* **146**, 1–6.

TARTE, P., POTTIER, M.J., & PROCES, A.M. (1973) Vibrational studies of silicates and germanates – V. IR and Raman spectra of pyrosilicates and pyrogermanates with a linear bridge. *Spectrochimica Acta* **29A**, 1017–1027.

THOMPSON, J.B. (1978) Biopyriboles and polysomatic series. *American Mineralogist* **63**, 239–249.

TIMM, B.C. (1941) *The Geology of the Southern Cornudas Mountains, Texas and New Mexico*. M.Sc. Thesis, University of Texas, Austin, Texas.

VERRECCHIA, E.P. & LE COUSTUMER, M.-N. (1996) Occurrence and genesis of palygorskite and associated clay minerals in a Pleistocene calcrete complex, SDE Boqer, Negev Desert, Israel. *Clay Minerals* **31(1)**, 182–202.

VON KNORRING, O. & FRANKE, W. (1987) A preliminary note on the mineralogy and geochemistry of the Aris phonolite, SWA/Namibia. *Communications Geological Survey S.W. Africa/Namibia* **3**, 65.

VON KNORRING, O., PETERSEN, O.V., KARUP-MØLLER, S., LEONARDSEN, E.S., & CONDLIFF, E. (1992) Tuperssuatsiaite, from Aris phonolite, Windhoek, Namibia. *Neues Jahrbuch für Mineralogie Monatshefte* **4**, 145–152.

WANG, M.K., TSENG, P.C., CHANG, S.S., RAY, D.T., SHAU, Y.H., SHEN, Y.W., CHEN, R.C., & CHIANG, P.N. (2009) Origin and mineralogy of sepiolite and palygorskite from the Tuluanshan Formation, Eastern Taiwan. *Clays and Clay Minerals* **57(5)**, 521–530.

WARNER, L.A., HOLSER, W.T., WILMARTH, V.R., & CAMERON, E.N. (1959) Occurrence of nonpegmatite beryllium in the United States. *Geological Survey Professional Paper* **318**.

YAKOVENCHUK, V.N., IVANYUK, G.Y., PAKHOMOVSKY, Y.A., SELIVANOVA, E.A., & MIKHAILOVA, J.A. (2011) Ellingsenite, $Na_5Ca_6Si_{18}O_{38}(OH)_{136}H_2O$, a new martinite-related mineral species from phonolite of the Aris alkaline complex, Namibia. *Canadian Mineralogist* **47**, 1099–1107.

ZAPP, A.D. (1941) *Geology of the Northeastern Cornudas Mountains, New Mexico*. M.Sc. Thesis, University of Texas, Austin, Texas, United States.

Received August 14, 2019. Revised manuscript accepted May 23, 2020.